

# Evolution of accretor stars in massive binaries: broader implications from modeling $\zeta$ Ophiuchi

M. RENZO<sup>1,2</sup> AND Y. GÖTBERG<sup>3,\*</sup>

<sup>1</sup>*Department of Physics, Columbia University, New York, NY 10027, USA*

<sup>2</sup>*Center for Computational Astrophysics, Flatiron Institute, New York, NY 10010, USA*

<sup>3</sup>*The Observatories of the Carnegie Institution for Science, 813 Santa Barbara Street, Pasadena, CA 91101, USA*

## ABSTRACT

Most massive stars are born in binaries close enough for mass transfer episodes. These modify the appearance, structure, and future evolution of both stars. We compute the evolution of a 100-day period binary consisting initially of a  $25 M_{\odot}$  star and a  $17 M_{\odot}$  star, which experiences stable mass transfer. We focus on the impact of mass accretion on the surface composition, internal rotation, and structure of the accretor. To anchor our models, we show that our accretor broadly reproduces the properties of  $\zeta$  Ophiuchi, which has long been proposed to have accreted mass before being ejected as a runaway star when the companion exploded. We compare our accretor to models of single rotating stars and find that the later and stronger spin-up provided by mass accretion produces significant differences. Specifically, the core of the accretor retains higher spin at the end of the main sequence, and a convective layer develops that changes its density profile. Moreover, the surface of the accretor star is polluted by CNO-processed material donated by the companion. Our models show effects of mass accretion in binaries that are not captured in single rotating stellar models. This possibly impacts the further evolution (either in a binary or as single stars), the final collapse, and the resulting spin of the compact object.

*Keywords:* stars: individual:  $\zeta$  Ophiuchi – stars: massive – stars: binaries

## 1. INTRODUCTION

The overwhelming majority of massive stars is born in multiple systems (e.g., Mason et al. 2009; Almeida et al. 2017; Moe & Di Stefano 2017), and a large fraction will exchange mass or merge with a companion in their lifetime (e.g., Sana et al. 2012). The most common type of interaction is stable mass transfer through Roche lobe overflow (RLOF) after the end of the donor star’s main sequence (case B, Kippenhahn & Weigert 1967), when stars experience most of their radial expansion. Many studies have focused on the dramatic impact that these interactions have on the donor star (e.g., Morton 1960; Yoon et al. 2017; Götberg et al. 2017, 2018; Laplace et al. 2020, 2021; Blagorodnova et al. 2021). Often the accreting companion is treated as a point mass. However, binary interactions have a crucial impact on the initially less massive star too.

### 1.1. The importance of accretor stars

During mass transfer, the initially less massive star is expected to accrete mass, spin-up to critical rota-

tion (e.g., Packet 1981), and possibly be polluted by nucleary processed material from the inner layers of the donor star (e.g., Blaauw 1993). The increase in mass leads to growth of the convective core and consequent “rejuvenation” of the accretor star (e.g., Neo et al. 1977; Schneider et al. 2016). Understanding the evolution of accretor stars in massive binaries has wide and crucial implications for stellar populations, electromagnetic transient observations, and gravitational-wave progenitors.

Accretor stars can appear as blue stragglers (e.g., Chen & Han 2009, 2010; Rain et al. 2021) and thus impact cluster populations, their age estimates, and their main sequence (e.g., Pols & Marinus 1994; Wang et al. 2020) and post main sequence morphology (e.g., Wei et al. 2021). The high spin of the accretor star after mass transfer might be the dominant explanation for the origin of Oe and Be stars (i.e., hydrogen-rich stars showing emission lines, e.g., Pols et al. 1991, Bodensteiner et al. 2020, Vinciguerra et al. 2020, Dorigo Jones et al. 2020, Wang et al. 2021, Hastings et al. 2021, see Rivinius et al. 2013 for a review). Rotationally-mixed accretor stars at low metallicity have also been suggested to be impor-

\* Hubble Fellow

tant for the ionizing flux of high-redshift galaxies (e.g., Eldridge & Stanway 2012; Stanway et al. 2016).

After mass transfer, the majority of massive binaries will be disrupted by the first supernova, and eject the accretor star (“binary SN scenario”, Blaauw 1961; De Donder et al. 1997; Eldridge et al. 2011; Boubert & Evans 2018; Renzo et al. 2019; Evans et al. 2020). A small fraction of these would be sufficiently fast to become runaway stars, but the majority will be too slow to stand out in astrometric surveys. Assuming a constant star formation history, Renzo et al. (2019) estimated that  $10.1^{+4.6\%}_{-8.6\%}$  ( $0.5^{+2.1\%}_{-0.5\%}$ ) of O-type stars could be slow “walkaway” (runaway) accretor stars ejected after the companion’s core collapse. Therefore, presently single O-type stars, that accreted mass earlier on, contribute to the populations of field massive stars (e.g., Dorigo Jones et al. 2020).

Massive accretor stars are also important from the transients perspective: Zapartas et al. (2019) estimated that  $14^{+4\%}_{-11\%}$  of hydrogen (H) rich type II SNe come from progenitors that were ejected from a binary. The fact that they accreted mass before exploding can influence their helium (He) core mass and thus the explosion properties and the inferred progenitors (Zapartas et al. 2021). The high post-mass transfer rotation rate of accretor stars in binaries might have implications for the formation of long gamma-ray burst progenitors (e.g., Cantiello et al. 2007).

The majority of isolated binary evolution scenarios for gravitational-wave progenitors include a common-envelope phase during which a compact object is engulfed in the envelope of a star. This phase is initiated by the initially less massive star, which accreted mass from its companion before the formation of the first compact object (e.g., Belczynski et al. 2016; Tauris et al. 2017; Broekgaarden et al. 2021). That accretion of mass, before the formation of the first compact object, could significantly modify the internal structure of the star that will initiate the common-envelope (e.g., Law-Smith et al. 2020; Klencki et al. 2021). Specifically, the rotation rate, chemical composition, and innermost structure of the envelope (because of rejuvenation) is expected to differ from that of a single star.

Despite their importance, accretor stars in binaries have so far received relatively little attention, with the pioneering studies of Ulrich & Burger (1976); Hellings (1983, 1984), and Braun & Langer (1995) as notable exceptions. Large grids of accretor star models are lacking and most existing studies focus on lower mass systems (e.g.,  $M_1 \lesssim 16 M_\odot$  in van Rensbergen et al. 2011) or neglect the crucial impact of rotation (e.g., Sravan et al. 2019, but see also Wang et al. 2020). Only few mas-

sive accretor star models exist (e.g., Petrovic et al. 2005; Cantiello et al. 2007).

Modeling accretor stars requires following the coupled evolution of two rotating stars that exchange mass. Making robust predictions is challenging because of the large number of uncertain parameters that are necessary to model each individual star and their interactions. Population synthesis calculations based on single star models cannot include the effects of binary mass transfer on the internal structure, and rely on the implicit assumption that the accretor is sufficiently well described by a (possibly fast-rotating) single star model. Here, we compute detailed evolutionary models of both stars in a binary and compare our accretor star to rotating single star models to test these assumptions.

## 1.2. A prototypical example of an accretor: $\zeta$ Ophiuchi

The nearest O-type star to Earth,  $\zeta$  Ophiuchi ( $\zeta$  Oph) provides the opportunity to constrain massive binary evolution models, as it is believed to be the ejected accretor star from a binary system.  $\zeta$  Oph is located  $107 \pm 4$  pc from Earth (Neuhäuser et al. 2020, and references therein), and has the spectral type O9.5IVnn (Sota et al. 2014). It occasionally shows emission lines, making it an Oe star (Walker et al. 1979; Vink et al. 2009). Its surface rotation rate is extremely high, with most estimates of the projected rotational velocity from optical spectra exceeding  $v \sin(i) \gtrsim 400$  km s $^{-1}$  (corresponding to the “nn” in the spectral type, Zehe et al. 2018 and references therein). By comparing the observed  $v \sin(i) = 432 \pm 16$  km s $^{-1}$  to the theoretical breakup rotation, Zehe et al. (2018) constrained the inclination angle to  $i \gtrsim 56$  degrees. Using optical interferometry, Gordon et al. (2018) measured the centrifugal distortion of  $\zeta$  Oph, finding a polar radius of  $7.5 R_\odot$  and centrifugally increased equatorial radius of  $9.1 R_\odot$ , corresponding to a  $v \sin(i) = 348$  km s $^{-1}$ .

$\zeta$  Oph was originally identified as a runaway because of its large proper motion by Blaauw (1952). Unfortunately, the *Gaia* data for this object are not of sufficient quality<sup>1</sup> to improve previous astrometric results, but estimates of the peculiar velocity range in  $20 - 50$  km s $^{-1}$  (e.g., Zehe et al. 2018; Neuhäuser et al. 2020). The large velocity with respect to the surrounding interstellar material is also confirmed by the presence of a prominent bow-shock (e.g., Bodensteiner et al. 2018).

Because of its young apparent age, extremely fast rotation, and nitrogen (N) and He rich surface (e.g., Herrero et al. 1992; Blaauw 1993; Villamariz & Herrero

<sup>1</sup> The renormalized unit weighted error (RUWE) of this star in Gaia EDR3 is 4.48.

2005; Marcolino et al. 2009),  $\zeta$  Oph is a prime example of runaway from the binary SN scenario (Blaauw 1993). Many studies have suggested that  $\zeta$  Oph accreted mass from a companion before acquiring its large velocity, both from spectroscopic and kinematic considerations (e.g., Blaauw 1993; Hoogerwerf et al. 2000, 2001; Tetzlaff et al. 2010; Neuhäuser et al. 2020) and using stellar modeling arguments (e.g., van Rensbergen et al. 1996). Recently, Neuhäuser et al. (2020) suggested that a supernova in Upper-Centaurus-Lupus that occurred  $1.78 \pm 0.21$  Myr ago produced the pulsar PSR B1706-16, ejected the companion  $\zeta$  Oph, and also injected the short-lived radioactive isotope  $^{60}\text{Fe}$  on Earth. This argues strongly for a successful SN explosion of the companion with a  $\sim 250 \text{ km s}^{-1}$  natal kick, sufficient in most cases to disrupt the binary (e.g., Tauris 2015; Renzo et al. 2019; Evans et al. 2020).

Although the nature of  $\zeta$  Oph as a binary product is well established, previous attempts to model it rely purely on mixing due to rotation as explanation the N- and He-rich surface composition, because of its observed large surface rotation rate (e.g., Maeder & Meynet 2000). Also in binary models, chemical enrichment on the surface has been assumed to originate from the spin-up triggering rotational mixing which dredges up processed material from the stellar core (van Rensbergen et al. 1996, see also Cantiello et al. 2007). However, Villamariz & Herrero (2005) (hereafter, VH05) were unable to obtain a satisfying fit for the stellar spectra using the single-star rotating models from Meynet & Maeder (2000, 2003): by the time rotational mixing enriches the surface, single massive stars have significantly spun down through wind mass loss.

Models predict lower efficiency of rotational mixing for metal-rich and relatively low mass stars. The reason is the increased importance of mean molecular weight gradients and the longer thermal timescales compared to more massive stars (e.g., Yoon et al. 2006; Perna et al. 2014). The parent association of  $\zeta$  Oph, identified by Neuhäuser et al. (2020), has a metallicity  $Z = 0.01 \simeq Z_\odot$  (based on asteroseismology from Murphy et al. 2021) and mass estimates for  $\zeta$  Oph range from  $13 - 25 M_\odot$ . This mass is at the lower end of the range where rotational mixing is thought to be able to efficiently bring CNO-processed material to the surface (chemically homogeneous evolution, Maeder & Meynet 2000). Given the challenges in explaining the surface composition of  $\zeta$  Oph as a rotating, single star and the evidence for its past as a member of a binary system, this star offers a unique opportunity to constrain the evolution of accretors in massive binaries.

Here, we present self-consistent binary evolution models of the coupled evolution of both stars and their orbit. After describing our **MESA** setup in Sec. 2, we present a model which reproduces the majority of the salient features of  $\zeta$  Oph in Sec. 3. We show the binary mass transfer evolution in Sec. 4, before focusing on the accretor’s rotational evolution in Sec. 5 (compared to single stars in Sec. 5.2), and its internal mixing processes in Sec. 6 (again compared to single star models in Sec. 6.1). We discuss the sensitivity of our results to the many uncertain parameters in Sec. 7, before concluding in Sec. 8.

## 2. MODELING MASSIVE BINARIES WITH MESA

We follow the coupled evolution of two massive stars in a binary system using **MESA** (version 15140, Paxton et al. 2011, 2013, 2015, 2018, 2019). Our choice of input parameters is available at [https://github.com/mathren90/zeta\\_oph](https://github.com/mathren90/zeta_oph) and all our numerical results are available at <https://doi.org/10.5281/zenodo.4701565>. We discuss here only the most relevant parameters and describe the effects of varying some of the adopted values in Sec. 7. Appendix A gives more details on our choice of input physics, and in appendix B we discuss the numerical resolution.

We adopt the Ledoux (1947) criterion to determine convective stability and a mixing length parameter of 1.5. We allow for time-dependent convection as in Renzo et al. (2020) based on Arnett (1969). We include semiconvection and thermohaline mixing following Langer et al. (1983) and Kippenhahn et al. (1980), respectively, each with efficiency 1.0. We use the exponential core overshooting from Herwig (2000) with free parameters  $(f, f_0) = (4.25 \times 10^{-2}, 10^{-3})$  (Claret & Torres 2017) which broadly reproduces the width of the main sequence from Brott et al. (2011) for a  $16 M_\odot$  single star. We do not account for over/undershooting for off-center convective layers. We also use the local implicit enhancement of the convective flux in superadiabatic regions introduced in **MESA** 15140 (`use_superad_reduction = .true.`).

We treat rotation in the “shellular” approximation (e.g., Zahn 1992; Ekström et al. 2012), that is, we assume constant rotational frequency  $\omega$  along isobaric surfaces. Furthermore, we assume tidal synchronization and rigid rotation at the beginning of our runs, at the zero age main sequence (ZAMS). Our models include a diffusive approximation for meridional currents (Eddington-Sweet circulations, Sweet 1950), which dominate the chemical mixing due to rotation. We also include the secular and dynamical shear instabilities, and the Goldreich-Schubert-Fricke (GSF) instability (see Heger et al. (2000) for a review of these processes). We

assume a Spruit-Tayler dynamo for the transport of angular momentum (Spruit 2002), and choose the same parameters as Heger et al. (2000). This also includes the rotational enhancement of the wind mass loss as in Langer (1998). Moreover, when a star approaches critical rotation, we re-calculate the wind mass loss rate implicitly to keep its rotation sub-critical. Specifically, at each time step we calculate a wind enhancement factor to reach the ratio  $\omega/\omega_{\text{crit}} \lesssim 0.95$  where  $\omega$  is the angular spin frequency and  $\omega_{\text{crit}} = \sqrt{(1 - L/L_{\text{Edd}})GM/R^3}$  is the critical spin frequency, with  $L_{\text{Edd}}$  the Eddington luminosity computed using the stellar opacity down to optical depth  $\tau = 2/3$ ,  $L$  is the luminosity,  $R$  the radius of the equator, and  $G$  the gravitational constant.

We assume a metallicity of  $Z = 0.01$  informed by the present-day  $Z$  of  $\zeta$  Oph's parent cluster (Murphy et al. 2021). The relative element abundances are assumed to scale with solar values (Grevesse & Sauval 1998).

We include stellar winds following Vink et al. (2000, 2001) for effective temperature  $T_{\text{eff}} \geq 11\,000$  K, unless the surface H mass fraction is lower than 0.4, when we instead use the mass-loss rate from Nugis & Lamers (2000). For  $T_{\text{eff}} \leq 10\,000$  K, we use the mass-loss rate from de Jager et al. (1988), and interpolate linearly in between the hot and cold wind for intermediate  $T_{\text{eff}}$ . We assume a wind scaling factor of 1 (Smith 2014; Renzo et al. 2017).

Compared to the measurements for  $\zeta$  Oph, we might be over-estimating the wind mass-loss rate by a factor of 100 (“weak wind problem”, see Marcolino et al. 2009). This suggests that spin-down due to wind mass-loss may also be overestimated compared to reality. However, Lucy (2012) and Lagae et al. (2021) proposed that the temperature structure of the winds of low-luminosity O-type stars might affect the spectral lines and cause an empirical underestimate of the mass-loss rate.

We follow Kolb & Ritter (1990) to calculate the mass transfer rate with an implicit scheme. Moreover, we assume that the specific angular momentum and entropy of the transferred mass match the surface of the accretor, while the chemical composition is set by the stratification of the donor star. Mass transfer is conservative until the accretor reaches critical rotation, after which rotationally-enhanced mass loss governs the mass transfer efficiency (e.g., Petrovic et al. 2005). Transferred matter which is not successfully accreted carries away the specific angular momentum corresponding to the accretor’s orbital motion (e.g., Soberman et al. 1997; van den Heuvel et al. 2017).

For simplicity, we evolve the accretor star as single after the mass transfer is completed. We define this based on the surface properties of the donor star, specifically,

we require that it has lost most of its hydrogen-rich envelope – surface He mass fraction exceeds 0.35 – and its radius is smaller than both its Roche radius and the ZAMS radius. The stripped donor star is contracting at this point, and will likely develop strong wind mass loss, possibly appearing as a Wolf-Rayet star. Depending on the amount of leftover H-rich material and the wind mass-loss rate, it is possible that the donor would expand again later in the evolution, filling its Roche lobe anew (cf., Gilkis et al. 2019). However, this is not expected for the mass and metallicity we focus on here (e.g., Laplace et al. 2020). We stop the evolution of the accretor star at terminal age main sequence (TAMS) defined as when the central mass fraction of H drops below  $10^{-4}$ .

To compare with our accretor model, we also compute the main sequence evolution of non-rotating single stars of 15, 17, 20, 25, and  $30 M_{\odot}$  and four more single  $20 M_{\odot}$  stars rigidly rotating with  $\omega/\omega_{\text{crit}} = 0.2, 0.3, 0.4$ , and 0.5 at birth. Apart from the initial rotation rate and the fact that they are single, the setup of these models is otherwise identical to our stars in the binary system.

### 3. EVOLUTION OF AN ACCRETOR STAR

We describe here the evolution of a binary system in which the accretor can broadly reproduce the observed features of  $\zeta$  Oph. We assume initial masses  $M_1 = 25 M_{\odot}$ ,  $M_2 = 17 M_{\odot}$ , and initial orbital period  $P = 100$  days (corresponding to a separation  $a \simeq 314 R_{\odot}$ ) with a metallicity of  $Z = 0.01$ .

Fig. 1 shows the Hertzsprung-Russell (HR) diagrams of the donor (top) and accretor star (bottom) – see Fig. 8 for a single HR diagram with both stars. Each marker in the figure corresponds to an elapsed interval of 50 years.

After 7.24 Myr, the most massive star in the system evolves off the main sequence and  $\sim 8400$  years later, at point A in Fig. 1, it overfills its Roche lobe and starts to donate mass. This results in a stable case B RLOF on a thermal timescale from point A to F (black outline of the curves). We refer to Götberg et al. (2017); Klencki et al. (2020); Laplace et al. (2021); Blagorodnova et al. (2021) and references therein for a detailed description of the evolution of massive donor stars in binaries. Although our models are more massive, the qualitative behavior of the donor star is similar. Minor differences might arise because of mixing above and in the H-burning shell (e.g., Schootemeijer et al. 2019; Klencki et al. 2021), and its interplay with the mass transfer.

At the onset of RLOF (point A in Fig. 1), the accretor star is still on the main sequence with  $T_{\text{eff}} \simeq 10^{4.5}$  K and its central mass fraction of hydrogen is  $X(^1\text{H}) \simeq 0.42$ . The accretion of material drives the star out of ther-

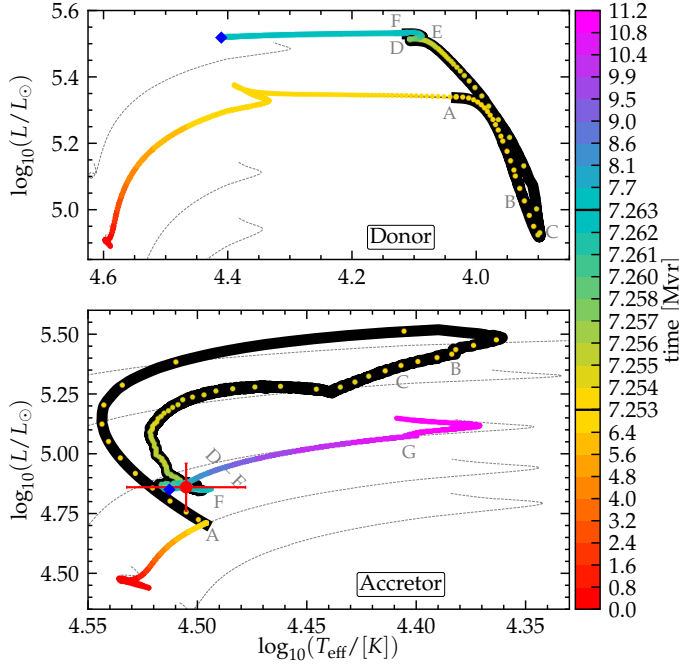


**Figure 1.** HR diagram for the donor star (top) and accretor star (bottom) of a model for an interacting binary star. Each point is separated by 50 years, and the black outline corresponds to the RLOF phase. The colors show the age on a non-uniform scale: we use smaller time-bins during RLOF ( $7.25 \text{ Myr} \lesssim t \lesssim 7.26 \text{ Myr}$ ). The red data point shows the estimated stellar properties of  $\zeta$  Oph according to VH05. The blue diamonds mark the end of the binary run, after which we continue to evolve the accretor as a single star from until TAMS, thus the bottom panel shows a longer time. We emphasize the different scales on the two panels. The thin gray dashed line show the main sequence evolution of non-rotating single stars of 15, 17, 20, 25, and  $30 M_\odot$  at  $Z = 0.01$  for comparison.

mal equilibrium and it quickly becomes over-luminous to radiate away the excess internal energy. The accretor reaches  $L \simeq 10^{5.5} L_\odot \gg L_{\text{nuc}} \simeq 10^{5.1} L_\odot$ , with  $L_{\text{nuc}}$  the total energy released per unit time by nuclear burning (integrated throughout the star). We note that because of the rejuvenation (see Sec. 6),  $L_{\text{nuc}}$  also increases from its pre-RLOF value. The duration of this phase is only  $\lesssim 2 \times 10^3$  years, corresponding roughly to the thermal timescale of the outer envelope of the accretor. During the same phase, the radius of the accretor increases dramatically from  $\sim 7.5 R_\odot$  to  $\sim 35 R_\odot$ .

At point B – close to the lowest  $T_{\text{eff}}$  – the accretor reaches critical rotation, which briefly decreases the efficiency of mass accretion. With lower mass accretion rate, the star can contract and heat up, causing the track to change direction. The contraction also increases  $\omega_{\text{crit}}$ , allowing for further accretion to resume.

At  $T_{\text{eff}} \simeq 10^{4.42} \text{ K}$ , slightly after point C, the inner layers of the donor’s envelope are exposed. These layers were part of the donor’s convective hydrogen-burning core earlier during the main sequence evolution, before the core receded in mass coordinate. Because this material has been exposed to the CNO cycle, the transferred material becomes progressively more enriched in helium and nitrogen. The difference in composition of the incoming material affects the opacity and mean molecular weight in the outer layers of the accretor and causes a kink in its evolutionary track, around  $\log_{10}(T_{\text{eff}}/\text{K}) \sim 4.45$ . Specifically, material with a high mean molecular weight  $\mu$  is placed on top of the comparatively low- $\mu$  envelope of the accretor. Because of the increasing gradient in mean molecular weight, thermo-haline mixing starts in the outer layers of the accreting star, and, together with rotational mixing, it progressively dilutes the surface  ${}^4\text{He}$  and  ${}^{14}\text{N}$  mass fractions (we discuss further mixing processes and the internal composition of the accretor in Sec. 6). The numerical treatment of these mixing processes causes noisy features from point D to F on the HR diagram of the accretor (e.g., Cantiello et al. 2007).

From D to E the donor star expands again: by point D the surface is He-rich, and partial recombination of  ${}^4\text{He}$  drives a convective layer which has extremely low mass ( $\lesssim 10^{-4} M_\odot$ ) but can expand to large radii<sup>2</sup>.

Accounting for both wind mass loss and the amount of mass transferred, at the end of our binary run (blue diamonds in Fig. 1) the donor becomes a helium star of  $\sim 9.4 M_\odot$ , likely to contract further. Depending on its wind mass-loss rate, the stripped donor star’s spectrum is expected to show absorption lines, emission lines, or a mixture of both (e.g., Crowther 2007; Massey et al. 2014; Neugent et al. 2017; Götberg et al. 2018; Shenar et al. 2020). Its surface H mass fraction is  $\lesssim 0.2$  and this residual H-rich layer could be removed by further wind mass loss (e.g., Yoon et al. 2017; Götberg et al. 2017; Laplace et al. 2020).

We emphasize that our adopted (standard) choices to model mixing and rotation are likely to impact the morphology of the accretor’s evolutionary track during RLOF. The entire duration of RLOF from A to F is only about  $10^4$  years – of the order of the thermal timescale of the donor star. Moreover, the accretor spends most of this time close to the final, post-RLOF position (blue diamond in the bottom panel of Fig. 1). Therefore, the

<sup>2</sup> With previous MESA releases, we found it challenging to compute models beyond this phase: the large increase in radius impacts significantly the mass transfer rate.

direct observation of a (population of) mass-transferring binary(ies) is unlikely.

### 3.1. Mass, velocity, photometry, and age of $\zeta$ Oph are naturally explained by binary interactions

At the end of our binary evolution, well after the donor detaches from its Roche lobe (blue diamonds in Fig. 1) the accretor is a H-rich fast-rotating star of  $\sim 20.1 M_{\odot}$ . This matches well with the estimates for  $\zeta$  Oph, which although highly uncertain, typically include  $20 M_{\odot}$  in their range (e.g., Hoogerwerf et al. 2001, VH05, Neuhäuser et al. 2020).

The post-RLOF orbital velocity of the accretor is  $v_2 \simeq 52 \text{ km s}^{-1}$ . In the subsequent evolution, wind mass loss from both stars will widen the binary and decrease the orbital velocity of the accretor star. As a test, we evolved one binary assuming the Nugis & Lamers (2000) wind mass loss rate for the stripped donor until its He core depletion. At that point the accretor star's orbital velocity has decreased to  $\sim 40 \text{ km s}^{-1}$ , and it is expected to decrease even further during the remaining evolution. The precise amount of the orbital widening and decrease of the accretor's orbital velocity depends on the uncertain stripped star mass loss rate (e.g., Vink 2017; Sander & Vink 2020). Nevertheless, the value we obtain for the orbital velocity of the accretor is in broad agreement with estimates of the observed runaway velocity of  $\zeta$  Oph.

In the evolution beyond the blue diamond in Fig. 1 (computed as a single star) the accretor settles on a main-sequence track at higher luminosity compared to the original track because of the accretion of mass, and its slope is slightly steeper due to the close-to-critical rotation and the accretion of partially nuclear processed (He- and N-rich) material.

The effective temperature, bolometric luminosity, and kinematic age of  $\zeta$  Oph are also reasonably well reproduced by our model (cf. Fig. 1). After detachment, the donor star has approximately 0.5 Myr left until core-collapse, which likely will disrupt the binary system and eject the accretor star (e.g., Renzo et al. 2019). As indicated by the colors of the track in Fig. 1, our accretor model spends around 2 Myr within the error bars for  $\zeta$  Oph estimated by VH05. This means that after the companion explodes, the accretor star will look similar to  $\zeta$  Oph for around 1.5 Myr, in good agreement with the estimated time of  $1.78 \pm 0.21$  Myr since  $\zeta$  Oph was unbound from its companion (Neuhäuser et al. 2020).

According to our model, the present-day age of  $\zeta$  Oph is  $\sim 7.5 - 9.5$  Myr. The age of the parent association of  $\zeta$  Oph, Upper-Centaurus-Lupus, is relatively uncertain, with estimates from pre-main sequence isochrone fitting

of about  $9 \pm 1$  Myr, but an average age of  $15 \pm 3$  Myr (Pecaut & Mamajek 2016). Given the sensitivity of our model to mixing processes and rejuvenation (see also Sec. 6), the large age scatter of the region, and the possible systematics in age measurements, we consider our model broadly compatible with the existing constraints.

We discuss in detail the mass and mass-transfer evolution in Sec. 4, the internal and surface rotation in Sec. 5, and the chemical composition in Sec. 6. As a summary, the accretor in our binary starts with  $17 M_{\odot}$  and accretes about  $3.4 M_{\odot}$  material during mass transfer (out of  $\sim 10.6 M_{\odot}$  total transferred). This causes rejuvenation: our accretor reaches  $T_{\text{eff}} = 32\,000 \text{ K}$  (the  $T_{\text{eff}}$  of  $\zeta$  Oph estimated by VH05) at  $\sim 7.3$  Myrs while a single initially  $20 M_{\odot}$  star would reach such temperature at  $\sim 6.5$  Myr. Moreover, our accretor reaches TAMS after 11.2 Myr, similar to the lifetime of a non-rotating single star of  $17 M_{\odot}$ , which is  $\sim 11.1$  Myr with our setup. Initially  $20 M_{\odot}$  rotating models have a main-sequence lifetime of  $\sim 9.2\text{--}9.6$  Myr (longer for higher initial rotation rates). After mass the mass transfer, the accretor star spins rapidly (see Sec. 5.1), and its surface composition is determined by the accretion of material from the donor star, which is progressively mixed inwards in the accretor (see Sec. 6.2). We find that the rotation and surface composition of  $\zeta$  Oph are more easily explained by accretor models than single rotating stars (e.g., VH05).

## 4. MASS AND MASS-TRANSFER RATE EVOLUTION

Fig. 2 shows the mass evolution (top panel) and the rate of mass change (middle and bottom panels) for each individual star during the mass transfer phase. The donor star (middle panel) loses mass via RLOF ( $\dot{M}_{\text{RLOF}} < 0$ , cyan line) and wind ( $\dot{M}_{\text{wind}} < 0$ , thin red line). The dashed blue line shows the sum of these two negative terms and represents the total rate of mass change of the donor. Conversely, the accretor (bottom panel) gains mass via RLOF (i.e.,  $\dot{M}_{\text{RLOF}} > 0$  from the accretor's point of view), but still loses mass to the wind ( $\dot{M}_{\text{wind}} < 0$ ). At peak (point C), the mass transfer rate reaches above  $10^{-2} M_{\odot} \text{ yr}^{-1}$  and taps into the optically thick matter of the donor (i.e., the donor's Roche radius becomes smaller than its photosphere  $R_{\text{RL},1} < R_1$ ).

Between point A and B, the mass transfer rate equals the mass accretion rate (bottom panel of Fig. 2), that is, initially the accretion is (by construction) fully conservative. The bulk of the accreted mass –  $\sim 2 M_{\odot}$  out of  $\sim 3.1 M_{\odot}$  – is accreted during this phase, which lasts about  $\sim 2 \times 10^3$  years. As the mass and surface rotation rate of the accretor increase, the adopted enhance-

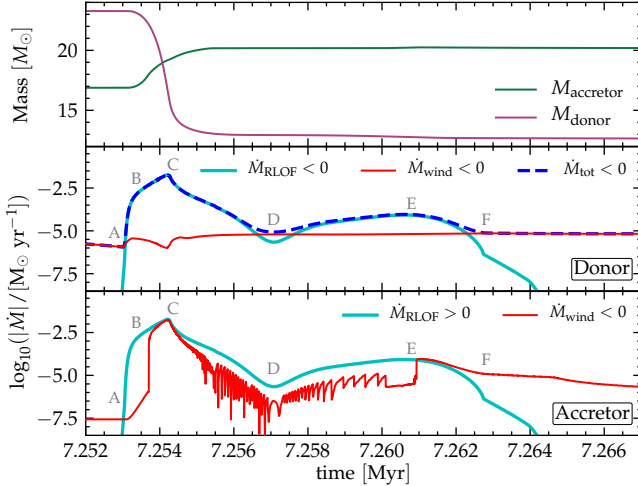


**Figure 2.** The top panel shows the total mass of each star as a function of time during RLOF. The middle and bottom panel show the contributions to the rate of mass change for the donor and accretor star, respectively. The cyan solid lines show the mass transfer rate due to RLOF, the red lines show the wind mass loss rates, which is mechanically enhanced for the accretor during mass transfer. In the middle panel, the dashed blue lines shows their sum, corresponding to the total mass loss rate of the donor. During RLOF the accretor reaches critical rotation, which leads to numerical oscillations in the rotationally-enhanced wind mass loss.

ment of the wind due to rotation progressively increases the mass-loss rate by  $\sim 5$  orders of magnitude. This mechanically-enhanced wind controls the accretion efficiency, and at  $\sim 7.254$  Myr (from B to C, where the red solid line and the cyan line overlap) the mass transfer becomes briefly non-conservative. In our setup, the majority of the mass that is transferred during this phase is ejected as a fast wind from the accretor, carrying the same specific angular momentum as the orbit of the accretor star. The decreased accretion efficiency allows the accretor to contract. In the remaining evolution from C to F, the interplay between the wind mass loss rate, the spin-up due to accretion and the spin-down due to inward transport of angular momentum (see Sec. 5) cause numerical oscillations in the wind mass loss rate. Nevertheless, for most of the evolution, accretion still occurs, albeit not-fully conservatively. This allows for CNO-processed material from the donor to reach the surface of the accretor during late stages of mass transfer.

The minimum of the mass transfer rate in point D corresponds to a brief phase of contraction (see also Fig. 1). However, from D-E, the donor star expands again. This is due to the partial recombination of the now He-rich outer layers, which causes a transient surface convection layer. The convective layers expand, leading to an increase in the mass-transfer rate, despite at this point the

binary is widening. During this phase, the mass transfer becomes highly non-conservative again (in the bottom panel the wind and the mass accretion rate nearly cancel each other again at  $\sim 7.261$  Myr), until the donor completely detaches from its Roche lobe at point F.

## 5. ROTATION AND ANGULAR MOMENTUM TRANSPORT IN THE ACCRETOR

### 5.1. Surface rotation

Rapid rotation is one of the main properties expected as a result of mass accretion (Packet 1981). One of the main distinguishing features of  $\zeta$  Oph is its extremely high surface rotation rate. The black line in the top panel of Fig. 3 shows the evolution of the surface equatorial rotational velocity  $v_{\text{eq}}$ <sup>3</sup> for our accretor

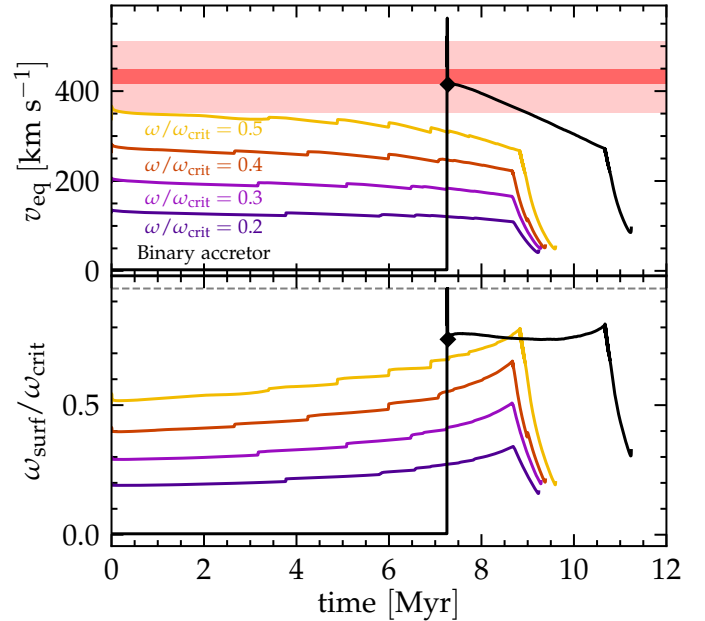


**Figure 3.** Equatorial surface rotational velocity (top panel) and  $\omega/\omega_{\text{crit}}$  (bottom panel) for the accretor model (black) and single rotating  $20 M_{\odot}$  stars (colored lines). The red bands in the top panel correspond to the  $v \sin(i)$  observed for  $\zeta$  Oph (see text). At  $\sim 7.25$  Myr the mass transfer quickly spins up the accretor to critical rotation: the dashed horizontal line in the bottom panel shows the upper-limit we impose. By the time the donor detaches from the RLOF the accretor is still spinning at  $\sim 400 \text{ km s}^{-1}$ . From this point (diamonds) onwards, we continue the evolution as a single star, and the accretor spins down because of wind mass loss. Note however that we use the wind mass-loss rate from Vink et al. (2000, 2001), which is suggested to be overestimated  $\sim 2$  orders of magnitude (Marcolino et al. 2009).

<sup>3</sup> More precisely,  $v_{\text{eq}}$  is a mass-weighted average of the equatorial rotation velocity for the layers with optical depth  $\tau \leq 100$ .

model, not including any projection effect. In the top panel, the dark horizontal red band shows the velocity  $432 \pm 16 \text{ km s}^{-1}$ , which is the  $v \sin(i)$  measured for  $\zeta$  Oph by Zehe et al. (2018). The lighter red band shows a range of 5 times their error bar, which roughly encloses the majority of the estimated  $v \sin(i)$  for  $\zeta$  Oph in the literature  $350 \text{ km s}^{-1} \lesssim v \sin(i) \lesssim 600 \text{ km s}^{-1}$  (e.g., Gordon et al. 2018 and Walker et al. 1979, respectively). For comparison, the colored solid lines show also  $v_{\text{eq}}$  for models of rotating  $20 M_{\odot}$  single stars with birth spins of  $\omega/\omega_{\text{crit}} = 0.2, 0.3, 0.4$  and  $0.5$ . We note that the “steps” in these lines are numerical artifacts which do not impact our results. The bottom panel of Fig. 3 shows the ratio of the surface rotational frequency  $\omega_{\text{surf}}$  to the critical rotational frequency  $\omega_{\text{crit}}$ .

The initial binary is wide enough that assuming tidal synchronization at ZAMS implies a very low  $v_{\text{eq}} \lesssim 3 \text{ km s}^{-1}$ . At 7.25 Myr, mass transfer rapidly spins up the accretor to critical rotation,  $v_{\text{crit}} \sim 520 \text{ km s}^{-1}$ . This corresponds to  $\omega/\omega_{\text{crit}} \simeq 0.95$  (dashed horizontal line in the bottom panel of Fig. 3), which is the upper-limit we impose in our models (see Sec. 2).

The star remains fast rotating during the mass transfer phase, and throughout the remaining evolution in a binary, which ends at the black diamond in Fig. 3 (corresponding to the blue diamonds in Fig. 1). Afterwards, the star spins down progressively because of wind mass loss, and within  $\sim 2$  Myr its equatorial surface rotational velocity drops below  $\sim 350 \text{ km s}^{-1}$ .

Both the single star models and our accretor (after being spun up) evolve to higher  $\omega/\omega_{\text{crit}}$  because of the increase in stellar radii and corresponding decrease in  $\omega_{\text{crit}}$  (e.g., Langer 1998; Zhao & Fuller 2020). However, our accretor model remains at a higher  $\omega_{\text{surf}}/\omega_{\text{crit}} \simeq 0.75$  for a significantly longer time: the chance of observing a single rotating star at very high  $\omega_{\text{surf}}/\omega_{\text{crit}}$  is lower than for an accretor from a massive binary system. Moreover, the  $\omega_{\text{surf}}/\omega_{\text{crit}}$  we find is in good agreement with the observationally constrained values for typical Oe and Be stars (see Rivinius et al. 2013, for a review).

Close to the end of the main sequence, the increase in wind mass loss rate as the stars cross the bistability jump (due to iron recombination at  $T_{\text{eff}} \simeq 25\,000 \text{ K}$ , e.g., Vink et al. 2000) strengthens the surface spin-down. This effect is also seen in the late main-sequence evolution of single stars rotating rapidly at birth.

Fig. 3 shows that our model retains a significant surface rotation for a long period of time, comparable to the kinematic age of  $\zeta$  Oph. Since the spin up of the accretor happens roughly half-way through its main sequence, the star is much faster rotating than single stars of the same mass, but which were initialized as fast ro-

tators at ZAMS. Although Fig. 3 does not account for the projection angle,  $i$ , Zehe et al. (2018) argued for  $i \geq 56$  degrees, corresponding to an upward shift of the red band in Fig. 3 of  $\lesssim 20\%$ . This shift impacts the comparison of  $\zeta$  Oph to our accretor model and to single star models in the same way.

We emphasize that our model is computed using the Vink et al. (2000, 2001) wind mass-loss rate with full efficiency throughout its evolution. This is two orders of magnitude higher than the wind mass loss rate reported by Marcolino et al. (2009) (weak wind problem, however, see also Lucy 2012; Lagae et al. 2021). While this may impact the evolution of the binary even before RLOF, it presumably increases the spin-down rate of our model compared to the observations. We expect that an accreting star modeled with lower wind-mass loss rate after mass transfer would retain an even higher surface rotation for longer (see also Sec. 7.1).

## 5.2. Internal rotation – comparison to single stars

Our model suggests that the internal rotational profile of accretor stars evolve differently compared to those of rotating single stars. To illustrate the angular momentum transport in our accretor star, it is again helpful to compare with single rotating  $20 M_{\odot}$  models.

The top row of Fig. 4 shows the internal rotational velocity,  $v_{\text{rot}} = \omega \times r$ , while the bottom row shows the angular frequency profile  $\omega$  as a function of mass coordinate. The first four panels in each row show single rotating stars with increasing initial  $\omega/\omega_{\text{crit}}$  and the last panels show our accretor model. The gray area in the rightmost panels highlights matter accreted during RLOF, while the colors of the lines indicate the age of the star for each profile that is shown.

The thin dashed lines in each panel of the top row of Fig. 4 mark the TAMS surface rotation rates: all our single star models reach a TAMS surface  $v_{\text{eq}} \simeq 50 - 60 \text{ km s}^{-1}$  (see Fig. 3). Initially faster rotating models spin down more in their outer layers and have slightly longer main sequence lifetimes (because of rotational mixing increasing the available fuel). As the core contracts and spins up, the single star profiles show a slight progressive development of a core-envelope interface.

Conversely, the entire interior of the accretor has a negligible rotational velocity until RLOF (starting at  $\sim 7.25$  Myr). Because of binary mass transfer, the accretor is spun up from the surface inwards (cf. initially rigid rotation assumed for single stars, Maeder & Meynet 2000), late in its evolution (cf. at ZAMS for single stars), and it reaches critical rotation  $\omega/\omega_{\text{crit}} \simeq 1$ . In our model, inward transport of angular momentum creates



**Figure 4.** Internal rotational velocity (top) and frequency (bottom) profile and for 20 M $_{\odot}$  single star models with increasing  $\omega/\omega_{\text{crit}}$  at birth (first four panels), and for the accretor of our fiducial binary. As in Fig. 1, the colorbar shows stellar age and is non-uniform. In the top (bottom) panel the thin dashed black lines mark the surface rotation rate (surface rotation frequency) at the end of the main sequence (TAMS). In the rightmost panels, the gray areas indicate mass accreted during mass transfer. The pink lines (structure at TAMS) in the last panel show that the core of the accretor is rotating almost as fast as its surface despite its much smaller radius, and both are rotating faster than the surface of the single star models.

a  $v_{\text{rot}}$  profile monotonically decreasing from the surface to the center. After the end of mass transfer, roughly at 7.27 Myr, the accretor achieves rigid and close to critical rotation (flat profiles in the last panel on the bottom row of Fig. 4,  $\omega \sim 6 \text{ day}^{-1}$ ). At the end of our binary run the accretor is still rigidly rotating, which persists<sup>4</sup> for a total duration of  $\sim 10^4$  years. Afterwards, the accretor's envelope spins down because of winds and its evolutionary expansion. By the end of the accretor's main sequence, the surface still spins with  $v_{\text{rot}} \simeq 100 \text{ km s}^{-1}$ , which is approximately twice as fast as the single star models.

Conversely, in the remaining evolution, the core contracts (decrease in  $r$ ). The weak core-envelope angular momentum coupling provided by the Spruit-Tayler dynamo leads to an approximately constant total angular momentum in the core, therefore, as it contracts and decreases its moment of inertia, its rotation rate  $\omega$  increases. At the end of the main sequence, the outer edge of the core of the accretor star has a similar rotational velocity as the surface, and much larger than for the single star models. Consequently, the TAMS core-envelope interface for the accretor is much more prominent than for in single rotating stars. It might be possible to distinguish accretors from initially single stars by using asteroseismology to measure the core rotation rate (e.g., Cantiello et al. 2014). However, this requires the detection of mixed modes which is presently challenging for massive stars.

Moreover, the higher core spin of accretors may have important implications for their future explosions (e.g., MacFadyen & Woosley 1999; Cantiello et al. 2007), the spin of the resulting compact objects, and the analysis of gravitational-wave events (for systems other than the progenitor of  $\zeta$  Oph, which remain bound and can evolve into gravitational wave mergers, e.g., Zaldarriaga et al. 2018; Qin et al. 2018; Callister et al. 2020).

## 6. MIXING AND COMPOSITION OF THE ACCRETOR

Rotational mixing and thermohaline mixing induced by the accretion of CNO-processed material affect significantly the composition profile of our accretor star. They both act primarily in the envelope, starting from the surface and growing inwards. MESA treats mixing using a diffusion approximation (Paxton et al. 2011), and to illustrate the dominant processes we show in Fig. 5 the diffusion coefficients for the mass fractions

<sup>4</sup> To calculate the duration, we consider rotation to be rigid if the difference between the minimum and maximum frequency throughout the star is  $\Delta\omega \lesssim 10^{-2} \text{ days}^{-1}$ .

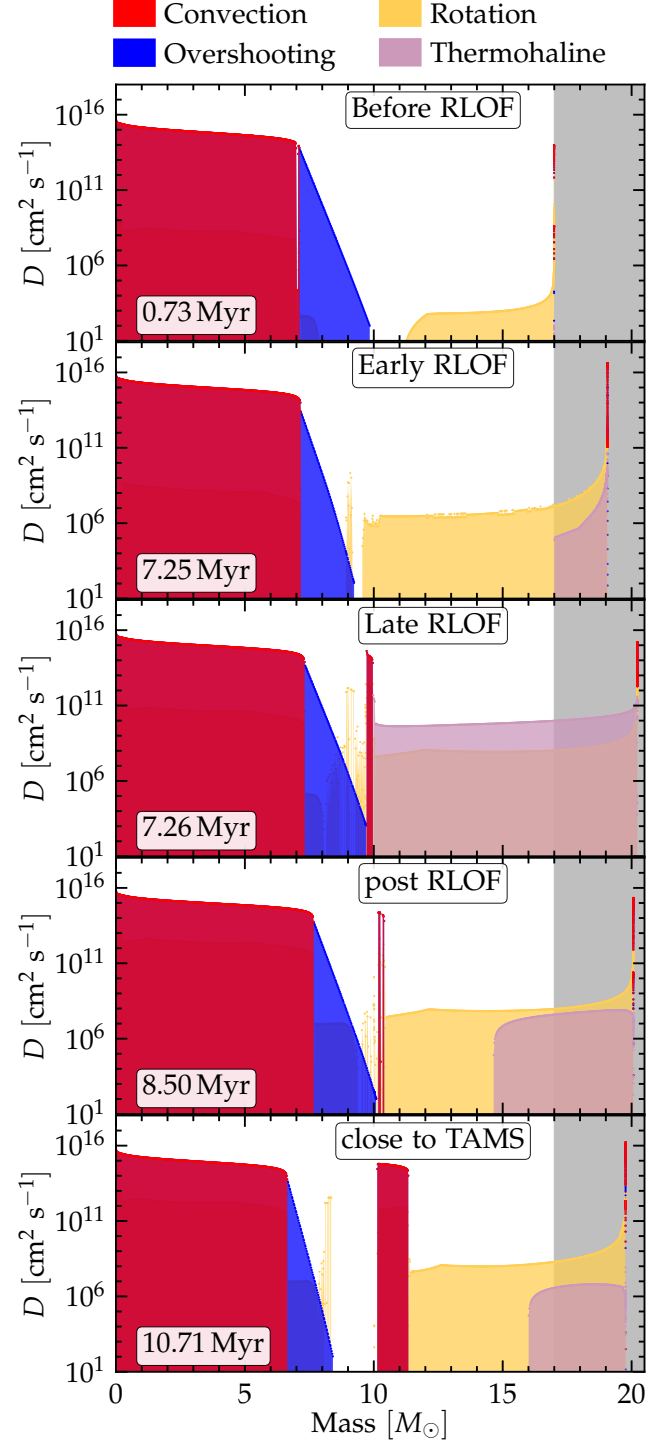


**Figure 5.** Mixing diffusion coefficients in the accretor star as a function of mass (the center corresponds to abscissa 0 and the surface to the maximum abscissa for which a diffusion coefficient is plotted). The gray area on the right highlights accreted material. From top to bottom, each panel shows a profile during the main sequence (before point A in Fig. 1), early during RLOF (slightly after point C), late during RLOF (close to point F), after detachment (within the  $\zeta$  Oph errorbar on Fig. 1), and after RLOF (point G). A movie of the entire evolution is included in Fig. 11.

of elements as a function of Lagrangian mass coordinate at selected times. In each panel of Fig. 5, the gray background highlights mass coordinates exceeding the initial mass of the star, reached because of accretion. The remaining colors show convection (red), overshooting (blue), rotational mixing (yellow), and thermohaline mixing (pink). Rotational mixing includes all the rotational instabilities that we consider – meridional currents, secular and dynamical shear instabilities, and GSF instability. However, throughout the evolution the meridional currents (Eddington-Sweet circulations) dominate. The only exception is at the interface between core and envelope (i.e., at the outer edge of the overshooting region), where significant dynamical shear and GSF mixing occur. For clarity, we do not show semiconvection which never dominates the mixing in our accretor model.

The top panel shows the typical structure of a main sequence massive star: the convective core initially reaching  $\sim 7 M_{\odot}$  with the overshooting extension to  $\sim 9 M_{\odot}$ . The slow initial rotation causes a very weak meridional circulation in the envelope. Meridional circulations are also present in the core throughout the evolution, but with a diffusivity more than nine orders of magnitude lower than core convection. A small sub-surface convective zone is also appreciable at the very surface (see, e.g., Cantiello et al. 2021).

In the second panel from the top (slightly after point C), the star has already accreted  $\sim 2 M_{\odot}$  (extending in the gray region), including some CNO-processed material from the layers close to the core of the donor star, and its surface is already spun up to  $\sim 330 \text{ km s}^{-1}$ . Thermohaline mixing has started in the newly accreted layers, but it is subdominant compared to rotational mixing due to meridional circulations in the envelope. Angular momentum transport (by the Spruit-Tayler dynamo) has already imparted some rotation to the inner layers of the envelope. This leads to the disconnected spike in rotational mixing at the outer edge of the core (at mass coordinate  $\sim 9 M_{\odot}$ ), dominated by dynamical shears. We note that between the top panel and the onset of RLOF, the convective core recedes in mass coordinate, but, by the time shown in the second panel, the accretion of mass has caused the core to grow back to its initial size.

In the third panel, the star has finished its mass accretion and is expelling the last transferred material (close to point F). Thermohaline mixing takes over the dominant role for chemical mixing in the envelope (although meridional circulations persist behind it, with a mixing coefficient two orders of magnitude smaller). The core is still growing in mass, meaning that rejuvenation is still

on-going. The mixing at the core-envelope boundary at  $\sim 9-10 M_{\odot}$  is partially still due to dynamical shear, but a thin, off-center, convective region also appears. Because we adopt an exponentially decreasing overshooting, the diffusion coefficient at the outer edge of the overshooting region is small, and therefore is the mixing between the core and the off-center convective region weak: this off-center convective region does not inject a significant amount of H-rich material in the core and is not participating significantly to the rejuvenation. We do not include over/undershooting for off-center convective layers, which could increase the coupling between these layers.

After detachment (fourth panel in Fig. 5, roughly corresponding to  $\zeta$  Oph’s structure today), thermohaline mixing is progressively shutting down from inside out as mass accretion has stopped, while meridional circulations remain active because of the rapid rotation. At this stage, the accreted material is well-mixed into the envelope of the accretor and there is no composition gradient in the outermost layers of the envelope.

Finally, the last panel displaying the interior mixing shortly before TAMS shows that, as the post-RLOF evolution proceeds, the previously thin, off-center convective layer grows thicker, including almost  $1.5 M_{\odot}$  of material between the mass coordinates  $10 - 11.5 M_{\odot}$ . In addition, the hydrogen-burning core has receded, leaving a  $\sim 1.5 M_{\odot}$  thick layer that is unaffected by mixing, meaning that the core and the convective layer have now completely disconnected.

A convective layer above the H-burning core during main-sequence evolution is uncommon for  $20 M_{\odot}$  single star models at  $Z=0.01$  (see, e.g., Schootemeijer et al. 2019 for lower metallicity and higher mass models showing off-center convective layers on the main-sequence). Apart from impacting the composition and density profile of the star, it is possible that it would also affect the future evolution of the star.

To illustrate the effect of the off-center convective layer that develops in the accretor model, Fig. 6 shows a comparison of the density profiles between the accretor model (point G in Fig. 1) and our four initially  $20 M_{\odot}$  single rotating stars when they reach the same central H mass fraction  $X_c = 0.085$  (close to TAMS). Convection significantly alters the density profile above the core of the accretor compared to the single rotating stars. The sharper inner density drop and shallower density profile of accretors may be possible to explore with asteroseismology:  $\zeta$  Oph itself has been observed to show non-radial pulsations (Walker et al. 2005), which may be involved in the transient appearance of emission lines and a decretion disk. If compared to a star of comparable

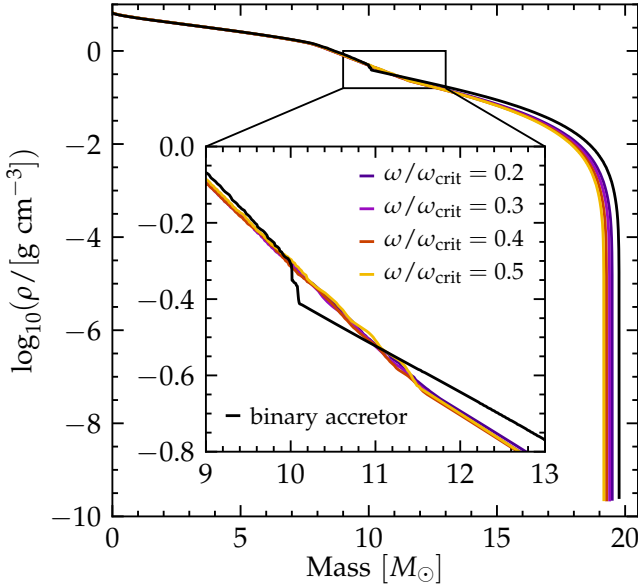


**Figure 6.** Comparison of the density profiles of the accretor model (black) and single  $20 M_\odot$  rotating stars (colors). The models are compared when they reach the same central H mass fraction of  $X_c = 0.085$  (point G in Fig. 1 for the accretor). The inset magnifies the region above the core, where the outcome of common envelope events is decided. A convective layer has altered the density profile of the accretor.

mass which evolved as single, the pulsations could shed light on the structural differences between single stars and binary products.

Moreover, for systems other than  $\zeta$  Oph's progenitor, if the binary remains bound after the explosion of the donor and the evolutionary expansion of the accretor leads to the development of a common envelope (e.g., Paczynski 1976), the layer above the He core is crucial for determine the success or failure of the common envelope ejection (e.g., Klencki et al. 2021). This might be crucial for our understanding of gravitational wave progenitors. Common envelope simulations have so far neglected the impact of previous mass accretion phase(s) on the density structure of the stars initiating the dynamically unstable mass transfer.

#### 6.1. Internal composition profile – comparison to single stars

In contrast to single rotating stars, our accretor model is chemically enriched both by accreting CNO-processed material and by outward mixing from its own core. Both these processes brings CNO-processed material to the surface, resulting in He- and N-enhancement.

However, these two mechanism tap into the core at different evolutionary phases, which can result in a different ratio of mass fractions  $X(^4\text{He})/X(^{14}\text{N})$  at the surface of an accretor star

compared single rotating stars. In fact, rotational mixing from the core occurs during the main sequence, as the  $^4\text{He}$  content is growing while the composition of  $^{14}\text{N}$  is fixed to the CNO-equilibrium abundance. Conversely, the material coming from the donor during a case B RLOF has a fixed (in time) composition. However, we emphasize that the ratio of abundances still varies with mass coordinate owing to the core recession in mass coordinate during the main sequence.

After RLOF, the surface  $^4\text{He}$  mass fraction of the accretor has increased by  $\sim 20\%$ , from 0.26 up to 0.31, while the surface  $^{14}\text{N}$  mass fraction has increased by a factor of 2.5, from  $5 \times 10^{-4}$  up to  $1.346 \times 10^{-3}$  (see also Tab. 1). This corresponds to a surface ratio  $X(^4\text{He})/X(^{14}\text{N}) = 231$ , which decreases in the remaining evolution. For comparison, this is slightly higher than TAMS ratio reached by our single star model starting with  $\omega/\omega_{\text{crit}} = 0.3$  which however reaches a similar  $X(^{14}\text{N})$  as our accretor model at TAMS (see below). Joint constraints on the He- and N-enhancement might thus be helpful to distinguish stars enriched by both the accretion of material from a companion and rotational mixing from stars self-enriched from their own primordial rotation, but the differences might be smaller than typical error bars on mass fractions derived from spectroscopy.

Because of its large change, we focus here on the  $^{14}\text{N}$  enrichment, but refer to Fig. 9 for the evolution of the mass fractions of  $^4\text{He}$ ,  $^{12}\text{C}$  and  $^{16}\text{O}$ . We also include a movie of the evolution of the accretor's internal composition profile for these four elements plus  $^1\text{H}$  in Fig. 10.

The first four panels of Fig. 7 show the mass fraction of  $^{14}\text{N}$  as a function of mass coordinate along the evolution of four  $20 M_\odot$  stars initialized with  $\omega/\omega_{\text{crit}} = 0.2, 0.3, 0.4, 0.5$ . The last panel of Fig. 7 shows our accretor model. The first four panels of Fig. 7 show typical rotational mixing profiles:  $^{14}\text{N}$  almost instantly reaches equilibrium in the core because of the efficient convective mixing in the CNO-cycle in the H-burning core, and it is then mixed outwards (as indicated by the arrows in the top left corner of each panel). The  $^{14}\text{N}$  profile is monotonically decreasing with mass coordinate, and the higher the initial rotation, the higher the surface  $^{14}\text{N}$  mass fraction reached at TAMS, because of the more efficient rotational mixing.

Conversely, the  $^{14}\text{N}$  mass fraction profile of the accretor is *not* monotonic throughout the evolution. This is because the profile is shaped by two main processes: (i) accretion of CNO-processed material from the donor

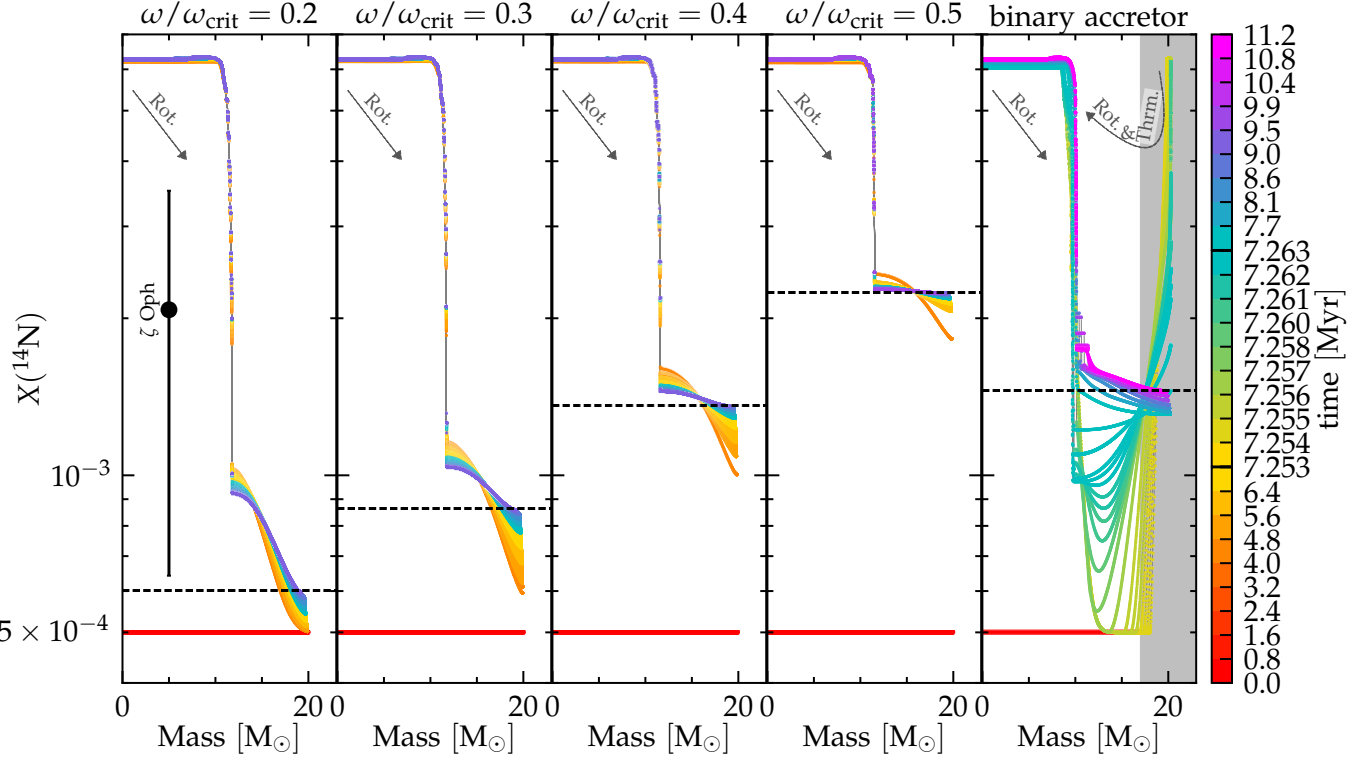


**Figure 7.**  $^{14}\text{N}$  mass fraction as a function of mass coordinate for  $20 M_{\odot}$  single star models with increasing  $\omega/\omega_{\text{crit}}$  at birth (first four panels), and for the accretor of our fiducial binary (last panel). The colors indicate stellar ages. In each panel, the red flat line marks the primordial value for  $Z = 0.01$ , the thin black dashed line marks the surface value at TAMS. In the last panel, the gray area highlights mass accreted during RLOF. The black errorbar in the first panel shows the surface  $^{14}\text{N}$  mass fraction of  $\zeta$  Oph estimated by VH05 assuming the surface mass fraction of H from Tab. 1. The abundance of  $^{14}\text{N}$  alone is not strongly constraining.

star, which is mixed inwards by thermohaline mixing and meridional circulations (as indicated by the top right arrow in the last panel), and (ii) outward mixing of the CNO-processed material from the accretor's receding main sequence core, brought outwards by rotational mixing – as in the single stars.

Initially, the tidally synchronized accretor star rotates too slowly ( $v_{\text{eq}} \lesssim 3 \text{ km s}^{-1}$ ) for rotational mixing to be efficient at mixing material outwards from the core. Therefore, until the onset of RLOF (roughly after 7.25 Myr) no appreciable variation of the envelope  $^{14}\text{N}$  mass fraction occurs. Late during RLOF, close to point F in Fig. 1, N-enriched material from layers above the donor's core piles onto the accretor's surface (inside the gray area in Fig. 7). At this stage, the close-to-critical rotation drive Eddington-Sweet circulations and the inversion in the mean molecular weight  $\mu$  make thermohaline mixing efficient. These mechanisms drive inward mixing of the accreted N-rich material, while rotational mixing bring N-rich material outwards, diluting it in the envelope (see also Fig. 5, third panel).

Simultaneously, the mere growth in mass causes the steepening of the core-temperature gradient and in-

crease in the convective core mass (rejuvenation, e.g., Schneider et al. 2016), driving some outward convective mixing of N-rich material. The evolution of the structure modified by accretion also causes the formation of an off-center convective region (cf. Fig. 5) which persists at least until TAMS, when we stop our model. Because the convective turnover timescale is much shorter than the main-sequence nuclear timescale, convection almost instantly homogenizes the composition of this region and produces “steps” at the outer edge of the core (slightly outside mass coordinate  $10 M_{\odot}$ ).

## 6.2. Comparison to $\zeta$ Oph’s composition, radius, and rotation rate

Tab. 1 summarizes the surface properties of the accretor star at 8.5 Myr (fourth panel of Fig. 5), roughly corresponding to  $\zeta$  Oph’s position on the HR diagram today. Both the mass and radius agree reasonably well with the estimates from VH05 and previous studies, that is  $20 M_{\odot}$  and  $8.3 \pm 1.5 R_{\odot}$ , respectively. Our radius of  $9.8 R_{\odot}$  is larger by  $\sim 0.6 R_{\odot}$  than the equatorial radius recently measured by Gordon et al. (2018), and our model has  $T_{\text{eff}} \simeq 31\,300 \text{ K}$ , on the lower end of the range

$M [M_\odot]$	$R [R_\odot]$	$\omega [\text{days}^{-1}]$	$v_{\text{rot}} [\text{km s}^{-1}]$	$X(^1\text{H})$	$X(^4\text{He})$	$X(^{12}\text{C})$	$X(^{14}\text{N})$	$X(^{16}\text{O})$
20.1	9.8	4.575	361.4	0.678044	0.312058	0.001339	0.001346	0.004149

**Table 1.** Surface properties of the accretor close to the present-day position of  $\zeta$  Oph on the HR diagram, corresponding to a physical age of 8.50 Myr, shortly after the end of RLOF (between the blue diamond and the lower estimate of  $\zeta$  Oph’s  $T_{\text{eff}}$  in Fig. 1, fourth panel of Fig. 5).

considered by VH05. The equatorial rotational velocity in excess of  $350 \text{ km s}^{-1}$  is also in the correct ballpark albeit possibly on the low end.

We report a surface H mass fraction<sup>5</sup> lower than initial because of the accretion of nuclearly processed material, and the surface mass fraction of the most prominent species  $^4\text{He}$ ,  $^{12}\text{C}$ ,  $^{14}\text{N}$ ,  $^{16}\text{O}$ . Assuming our surface H mass fraction  $X(^1\text{H})$ , the corresponding mass fractions of  $^4\text{He}$ ,  $^{12}\text{C}$ ,  $^{14}\text{N}$ ,  $^{16}\text{O}$  obtained by VH05 are  $0.34^{+0.14}_{-0.05}$ ,  $0.0006 \pm 0.0004$ ,  $0.002 \pm 0.001$ , and  $0.005 \pm 0.004$ .

In Fig. 7, the black errorbar in the first panel shows  $\zeta$  Oph’s surface  $^{14}\text{N}$  from VH05 (assuming the surface H mass fraction from our model listed in Tab. 1). The mass fraction of  $^{14}\text{N}$  alone is not sufficient to distinguish between these models, and already a moderate  $\omega/\omega_{\text{crit}} \geq 0.3$  is sufficient for models to reach the lower limit of the error bar.

By the accretor’s TAMS, rotational mixing (in the form of Eddington-Sweet circulations) and thermohaline mixing nearly homogenize the composition of the envelope of our accretor’s model. The surface mass fractions we obtain are sensitive to the interplay between several poorly understood processes treated in one dimension: mass accretion efficiency, rotationally enhanced wind mass loss, thermohaline mixing, and rotational mixing. These also impact the composition of the envelope, and thus its radius and  $T_{\text{eff}}$ . Therefore, although not perfect, we consider the match with the mass fractions reported by VH05 surprisingly satisfactory.

## 7. ROBUSTNESS OF THE MODELS AND DISCUSSION

Models of the interior evolution of stars require the use of several poorly constrained parameters, most arising from the one-dimensional representation of multi-dimensional phenomena (e.g., mixing, rotation, mass loss). This remains true when modeling two stars in a binary, with the added caveat that an even larger number of parameters enters in the treatment of binary interactions (and in particular mass transfer). This emphasizes the need for observational constraints and motivated us

to compare our models to the observationally well characterized  $\zeta$  Oph.

Accretor stars are expected in most populations of (massive) stars, both in clusters (e.g., Chen & Han 2009; Wang et al. 2020) and in the field (e.g., de Mink et al. 2011, 2013; Dorigo Jones et al. 2020). However, these might not obviously stand out as binary products in kinematics surveys (e.g., Renzo et al. 2019). Therefore, to inform the search for accretor stars in observed samples, it is also necessary to characterize the robustness of model predictions against numerical, physical, and algorithmic choices. In Sec. 7.1 we report on exploration of parameter variations for each individual star in the binary and our single star models. We discuss parameters governing the binary evolution Sec. 7.2, and the consequences of the assumed SN explosion of the companion in Sec. 7.3.

### 7.1. Uncertainties in the single-star physics

*Rotation*—Rotation is a critical ingredient of our models: it governs the equatorial radius and thus  $\omega/\omega_{\text{crit}}$ . Therefore, by assumption, it also controls the mass transfer efficiency through mechanical enhancement of the accretor’s wind (see Sec. 7.2). Through Eddington-Sweet meridional circulations, shear, and GSF instability, rotation contributes with outward mixing from the core, and more importantly inward mixing from the surface of the accretor. We emphasize that the shellular approximation used in one-dimensional stellar evolution codes might not be appropriate for  $\omega/\omega_{\text{crit}} \simeq 1$  (e.g. Maeder & Meynet 2000), which our accretor star reaches during RLOF. Decreasing the diffusion coefficient for Eddington-Sweet meridional circulations by a factor of 10 has a very small effect on the evolution of the accretor on the HR diagram. However, the noisiness during the late RLOF phase (beyond point B in Fig. 1) increases in amplitude, confirming that the details of this part of the evolution are sensitive to the treatment of rotational mixing (and its interplay with other processes).

*Angular momentum transport*—Our models assume a Spruit-Tayler dynamo (Spruit 2002) for the transport of angular momentum. Adopting the stronger transport from Fuller et al. (2019) might result in a more efficient spin-down of the surface during RLOF, possibly allowing for more accretion of mass.

<sup>5</sup> We obtain the mass fractions of individual elements inverting the definition  $\varepsilon(X) = 12 + \log_{10}(N_X/N_H)$ , where  $N_X$  and  $N_H$  are the number fractions of species  $X$  and H, respectively (e.g., Lodders 2019).

The accretor is spun up late and from the surface inwards. It also reaches critical rotation in contrary to the single star models, which are initialized at ZAMS with rigid rotation. Late during the mass transfer, even the weak core-envelope coupling of Spruit (2002) is sufficient for the accretor to achieve rigid rotation (see Fig. 4). Subsequently, the envelope spins down because of expansion and mass loss, and more importantly the core spins up because of its evolutionary contraction. We expect that following Fuller et al. (2019) the core would lose more angular momentum to the envelope, limiting its ability to spin up as it contracts and decreasing its rotational velocity. Nevertheless, we expect that the accretor star will be spun up from the surface and inwards, suggesting that the differences with single star rotational profiles may remain, albeit possibly smaller, because of the shorter evolutionary time left.

*Thermohaline mixing*—During RLOF, thermohaline mixing in the envelope becomes the dominant mixing process. In MESA, each mixing process is represented by its own diffusion coefficient, and they are then summed together (Paxton et al. 2011), under the implicit assumptions that mixing processes are independent from each other. This is typically reasonable since locally one process dominates the mixing. Initially, Eddington-Sweet circulations are dominant in the accretor’s envelope, however, later on, thermohaline mixing reaches and exceeds their diffusivity because of accretion of chemically enriched material from the donor. If fast rotation can physically modify thermohaline mixing processes, this could impact our accretor models. We also computed models with enhanced efficiency of thermohaline mixing (100 times higher, Schootemeijer et al. 2019), but these proved numerically unstable when accreting CNO-processed material.

*Convective overshooting*—On the basis of nucleosynthesis arguments (e.g., Herwig 2000) and asteroseismology (e.g., Moravveji et al. 2016), an exponentially decreasing overshooting is generally considered preferable. Nevertheless, we have also explored models with a step-function overshooting from Brott et al. (2011). Our exponential overshooting (Claret & Torres 2017) was chosen to reproduce the width of the main sequence of the models of Brott et al. (2011) and, not-surprisingly, the qualitative evolution of our fiducial model and models with step overshooting is similar. However, adopting a step overshooting provides a higher diffusivity at the outer edge of the core (cf. exponential decrease), which ultimately impacts the details of the chemical profile at the outer edge of the core, and the morphology of the evolutionary tracks during late RLOF.

*Stellar winds*— $\zeta$  Oph is one of the low-luminosity O-type stars for which Marcolino et al. (2009) found a lower-than-predicted wind mass loss rate. To address the “weak wind problem”, we also attempted running models with artificially decreased wind mass loss rate (e.g., Renzo et al. 2017), but these resulted in super-critically rotating ( $\omega/\omega_{\text{crit}} > 1$ ) post-RLOF accretor stars with untrustworthy numerical results. The solution to the “weak wind problem” is not currently known, but Lucy (2012) and Lagae et al. (2021) suggest that observed mass loss rates might be underestimated, meaning that the theoretically motivated hot star wind mass loss rate might still be appropriate to model low luminosity O-type stars.

Our models use the Vink et al. (2000, 2001) mass-loss rate on the main sequence, which includes the enhancement due to the bistability jump at  $T_{\text{eff}} \simeq 25\,000$  K. This results in the dramatic increase in the surface spin down at late times (cf. Fig. 3). However, the mass-loss (and consequently spin-down) enhancement at the bistability jump has recently been questioned by Björklund et al. (2021). If such enhancement does not occur, it is possible our models would retain a higher surface rotation rate, and higher  $\omega/\omega_{\text{crit}}$ . This would influence in a similar way our single star models and our accretor, suggesting the relative comparison between these models would still remain valid.

*Metallicity*—Throughout this study, we assumed an initial metallicity  $Z = 0.01$  informed by the asteroseismology of low mass stars in Upper-Centaurus-Lupus (e.g., Murphy et al. 2021), identified as the parent association for  $\zeta$  Oph by Neuhäuser et al. (2020). Moreover, we have assumed that mass fractions of each element scale with the Solar values (Grevesse & Sauval 1998), which might not be appropriate especially for massive stars (e.g., Grasha et al. 2021). With these assumptions, the initial mass fraction of  $^{12}\text{C}$  and  $^{14}\text{N}$  are lower than the values reported by VH05 for  $\zeta$  Oph (see Sec. 6.2). Even though both values increase during mass transfer, our model still slightly under-predicts them. Improved agreement could be obtained changing the ratio of abundances to non-solar values, or by changing the efficiency of downward rotational and thermohaline mixing which dilutes the accreted material into the accretor’s envelope.

We also ran a model identical to the one described in Sec. 3, except with  $Z = Z_{\odot} = 0.0142$  (Asplund et al. 2009) with the same composition scaling from Grevesse & Sauval (1998). Qualitatively, the binary evolution remains similar, with the higher metallicity stars having slightly larger radii and cooler  $T_{\text{eff}}$  at a given luminosity. This still produces a stable case B RLOF, however,

matching the high present-day  $T_{\text{eff}} = 32\,000 \pm 2\,000$  of  $\zeta$  Oph (e.g., VH05) requires more massive and hotter accretors at higher  $Z$  (see also Sec. 7.2).

### 7.2. Uncertainties in the treatment of mass transfer

*Mass transfer efficiency,  $\beta_{\text{RLOF}}$* —We regulate the accretion efficiency through the rotational enhancement of mass loss (e.g., Langer 1998; Petrovic et al. 2005; Wang et al. 2020). However, whether critical rotation can effectively stop the accretion of matter is unclear. Popham & Narayan (1991) and Paczynski (1991) argued that accretion of mass (but not angular momentum) might be possible even at or beyond critical rotation.

During RLOF, the total amount of mass lost by the donor is  $\Delta M_{\text{donor}} \simeq 10.6 M_{\odot}$ , of which only  $\Delta M_{\text{accretor}} \simeq 3.4 M_{\odot}$  are successfully accreted by the companion. This corresponds to an overall mass transfer efficiency  $\beta_{\text{RLOF}} \equiv |\Delta M_{\text{accretor}}|/|\Delta M_{\text{donor}}| \simeq 0.32$ , although the accretion efficiency is *not* constant throughout the mass transfer (e.g., van Rensbergen et al. 2006). In our models, the mass transfer efficiency depends on the radial and rotational evolution of the accreting star. During RLOF, the accretor is out of gravothermal equilibrium with significant impact on its radius and ultimately on the amount of mass transferred and its angular momentum. In reality, the gas stream between the two stars, the hot-spot due to the RLOF stream hitting the accretor’s surface (see below), and the geometric distortion of the outer layers because of the centrifugal forces would not follow the spherical symmetry imposed by 1D codes such as MESA.

While the mass-transfer efficiency,  $\beta_{\text{RLOF}}$ , and importantly its evolution need further attention, it is also likely that this parameter depends on the details of the system (masses, mass ratio, period, etc.). For instance, to explain the lower mass sdO+Be binaries found by Wang et al. (2021) it is likely that a larger mass transfer efficiency would be required. Conversely, Petrovic et al. (2005) argued for  $\beta_{\text{RLOF}} \simeq 0.1$  to reproduce WR+O star binaries.

Most studies, especially using rapid population synthesis tools, typically assume a constant  $\beta_{\text{RLOF}}$  and neglect the out-of-equilibrium phase of the accretor and how this can impact the binary and orbital evolution. Alternatively, rapid population synthesis can limit the accretion rate based on the thermal timescale of the accretor (calculated from models in gravothermal equilibrium). Based on this approach, Schneider et al. (2015) found a higher  $\beta_{\text{RLOF}} \simeq 0.7$  for a binary comparable to ours (initially  $M_1 = 20 M_{\odot}$ ,  $M_2 = 0.7M_1$  with separation  $a \simeq 300 R_{\odot}$ ), although their  $\beta_{\text{RLOF}}$  is very sensitive to the initial mass ratio and period in this regime.

*Specific angular momentum of accreted material*—This is an uncertain quantity and likely depends on the geometry of the accretion process, and in particular, whether the accretion stream through the first Lagrange point (L1) hits the accretor star directly, or if instead an accretion disk is formed (e.g., de Mink et al. 2013).

We calculate the minimum distance  $R_{\min}$  between the stream coming from L1 and the accretor using the fit from Ulrich & Burger (1976) to the numerical results of Lubow & Shu (1975). We find  $R_{\min} \simeq 1.5 R_{\odot} < R_{\text{accretor}}$ : this suggests that the stream should hit the accretor directly, without forming an accretion disk. Nevertheless, for the sake of numerical stability, we assume the incoming material and the accretor’s surface to have the same specific angular momentum. This provides a slow angular momentum accretion and consequent spin-up of the surface.

For a more physically motivated approach, we also attempted calculations using for specific angular momentum of the accreted material  $j = \sqrt{1.7GM_{\text{accretor}}R_{\min}}$ , representative for direct impact of the incoming stream with the accretor (Lubow & Shu 1975). This is typically much larger than the specific angular momentum of the accretor’s surface. However, these models proved numerically more unstable and providing less trustworthy results after the accretor is spun up significantly. In general, allowing for a faster accretion of angular momentum results in a faster spin-up, and a lower overall mass transfer efficiency  $\beta_{\text{RLOF}}$ .

*Specific entropy of the accreted material*—In our models, the composition of the transferred material is determined by the structure of the donor and the mass transfer rate calculated following Kolb & Ritter (1990), but we need to specify its specific entropy when it reaches the accretor surface. We follow the common practice of assuming the specific entropy of the incoming material to be same as the accreting surface. The scenario justifying this hypothesis is that during RLOF the matter is sufficiently optically thin so that radiative processes can rapidly equalize the entropy between the RLOF stream and the accreting surface. However, the very large mass-transfer rates we find (cf. Fig. 2) might result in optically thick flows for which this approximation might not be appropriate.

*Rejuvenation and core growth*—Because of the increase in mass, our accretor star is rejuvenated: its total main-sequence lifetime is longer than the lifetime of a single star born with the final post-RLOF mass of the accretor<sup>6</sup>

<sup>6</sup> But not significantly longer than the lifetime of a single star of its initial, pre-RLOF mass.

(e.g., Schneider et al. 2016). The rejuvenation is due to the increase - in mass - of the core region, which brings fresh nuclear fuel inwards. Our results are in agreement with Hellings (1983), while Braun & Langer (1995) did not find any rejuvenation in their accretor models. We attribute this difference to the lack of convective boundary mixing (e.g., overshooting, efficient semiconvection, shear) in their models, which impedes the growth of the core. In our models, the growth of the core is initially driven by convection and overshooting, and to a lesser extent by dynamical shear, while the off-center convective layer of Fig. 5 and Fig. 6 does not contribute significantly to the inward mixing of H-rich material and the rejuvenation itself. We cannot exclude that in the presence of a strong shell undershooting that convective layer would also mix efficiently with the core, enhancing further the rejuvenation effect.

*Initial binary parameters*—The initial donor mass  $M_1$ , mass ratio  $q \equiv M_2/M_1$ , and period of the progenitor binary of  $\zeta$  Oph cannot be directly constrained from observations. We have explored variation in these, and the qualitative behavior of the models is similar. Shorter initial periods results in larger post-RLOF orbital velocities, and thus larger runaway velocities if the binary is disrupted at the first SN (see Sec. 7.3). For example, taking  $P=75$  days (cf. 100 days in our fiducial model), the binary still experiences stable case B mass transfer, but the post-RLOF orbital velocity of the accretor is about  $60 \text{ km s}^{-1}$ , that is  $\sim 10 \text{ km s}^{-1}$  higher than in our fiducial model, because of the larger orbital velocity in the tighter binary system.

Increasing the donor mass also has a similar effect on the post-RLOF orbital velocity of the accretor. Using  $M_1 = 30 M_\odot$  (cf.  $25 M_\odot$  in Sec. 3),  $M_2 = 17 M_\odot$ , and  $P=100$  days, we obtain a post-RLOF velocity of  $65 \text{ km s}^{-1}$ . However, this produces a stripped donor of  $\sim 16 M_\odot$  at RLOF detachment, with stronger wind mass loss rate. Therefore this binary is expected to widen relatively more than our fiducial model of Sec. 3, slowing down the accretor. The increased mass of the stripped donor star could also imply a lower chance of exploding for the donor, which might instead collapse to a black-hole (however, see Sec. 7.3). This would be incompatible with the association of the pulsar PSR B1706-16 with  $\zeta$  Oph (Neuhäuser et al. 2020).

The higher  $M_1$  does not significantly change the post-RLOF total mass of the accretor, with  $M_2$  remaining about  $\sim 20.5 M_\odot$ , since in our models accretion is regulated mostly by the spin up of the accretor, and we do not couple the specific angular momentum of the transferred material to the orbit or the donor’s spin.

However, changing the initial mass ratio also changes the difference between the main-sequence lifetime of the two stars, and thus how far along the main sequence the accretor is at the onset of RLOF. The observed position of  $\zeta$  Oph on the HR diagram, particularly its relatively high  $T_{\text{eff}}$ , is difficult to reproduce assuming initially less massive accretors (which would remain too cool even after accreting mass), or a more equal initial mass ratio (which would produce an accretor that is too evolved and cool at the onset of mass transfer).

### 7.3. The explosion of the donor star

Throughout this study, we have assumed the “binary SN scenario” to explain the runaway nature of  $\zeta$  Oph: after the mass transfer phase, the explosion of the donor disrupts the binary and ejects the accretor at roughly its pre-explosion orbital velocity (e.g., Blaauw 1961; Eldridge et al. 2011; Renzo et al. 2019). This fate occurs to the majority of massive binary systems, and  $\zeta$  Oph might be the best example of it (e.g., Blaauw 1952, 1961; Hoogerwerf et al. 2000). Neuhäuser et al. (2020) suggested not only the companion successfully exploded producing the pulsar PSR B1706-16 and ejecting  $\zeta$  Oph, but also that the explosion produced radioactive  $^{60}\text{Fe}$  which polluted Earth.

From kinematic and orbital considerations they estimated the pulsar received a natal kick of  $253 \pm 54 \text{ km s}^{-1}$ , which would be sufficiently large to unbind the binary which has  $v_{\text{orb}} = \sqrt{G(M_1 + M_2)/a} \simeq 135 \text{ km s}^{-1}$  at the end of our binary simulation (blue diamond in Fig. 1), and this will decrease further in the remaining time to the donor’s core-collapse (Kalogera 1996; Tauris & Takens 1998; Tauris 2015).

The SN ejecta mass would depend on the post-RLOF wind mass loss of our donor star, which is uncertain (see also Renzo et al. 2017; Vink 2017; Gilkis et al. 2019; Sander & Vink 2020). At the end of our binary evolution simulation, our stripped donor is  $\sim 9.4 M_\odot$ , with a surface H fraction of  $X \lesssim 0.2$  for a layer of  $\Delta M \simeq 2.5 M_\odot$ . Its wind mass-loss rate is  $\sim 10^{-5} M_\odot \text{ yr}^{-1}$ , calculated assuming the empirical Wolf-Rayet wind mass loss prescription from Nugis & Lamers (2000, see also Fig. 2). We expect that the donor will explode in a H-free type Ib supernova. Although our stripped donor is rather massive, recent studies hints at a higher “explodability” of donor stars in binary systems (e.g., Schneider et al. 2021; Laplace et al. 2021; Vartanyan et al. 2021).

We have neglected the impact of the explosion on the structure of the accretor star. At the time of the explosion, the accretor subtends a solid angle  $\sim R^2/a^2 \simeq 2 \times 10^{-3}$  steradians with  $R$  the accretor radius and  $a$  the binary separation. We neglect the post-RLOF wind-

driven orbital widening for this estimate. The blast wave will hit the accretor causing mass loss – directly via ablation and by injecting energy in the envelope, inflating it and enhancing its wind (Wheeler et al. 1975; Tauris & Takens 1998; Podsiadlowski 2003; Hirai et al. 2018; Ogata et al. 2021). Because of the SN shock, the just ejected new runaway star might appear bloated and redder (long before it overtakes the slowing SN remnant). The impact of this brief out of thermal equilibrium phase on the stellar spin should be investigated further.

Using 2D hydrodynamic simulations of the star-SN ejecta interactions in close binaries ( $a \lesssim 60 R_\odot$ , cf.  $a \gtrsim 343 R_\odot$  in our fiducial binary model), Hirai et al. (2018) found that the companion star recovers its pre-explosion luminosity and effective temperature within a few years to decades. This result was later corroborated for a wider range of parameters by Ogata et al. (2021). The amount of mass removed by the SN shock is  $\lesssim 10^{-2} M_\odot$ . The SN ejecta might also pollute the surface of the runaway by depositing processed nuclear material (e.g., Przybilla et al. 2008; Suda et al. 2021). However, for the large final separation of our model, little pollution is expected and enhanced mass loss and inward mixing might quickly dilute any signature below detectable levels.

## 8. SUMMARY & CONCLUSIONS

The impact of mass transfer on the structure and evolution of accretor stars in massive binaries has received relatively little attention. To investigate this, we have performed **MESA** calculations of massive binaries evolving two coupled stars simultaneously.

As a first application, we focused on finding a model in which the accretor properties are in qualitative agreement with observations of the nearest O-type star to Earth. This is the runaway star  $\zeta$  Oph, which has long been suggested to be a former accretor star ejected from a binary at the core-collapse of the donor star (binary SN scenario, Blaauw 1961). However, our models are also informative for the generic population of massive stars accreting in binaries.

### 8.1. Reproducing $\zeta$ Oph

We found that the main features of  $\zeta$  Oph can be reasonably well reproduced using standard non-fine-tuned stellar physics assumptions for the treatment of mass transfer, chemical mixing, and rotation. Our choices are described in Sec. 2 and Appendix A.

Our fiducial model is a binary starting with  $M_1 = 25 M_\odot$ ,  $M_2 = 17 M_\odot$ , and  $P = 100$  days at metallicity  $Z = 0.01$  (see Sec. 3). This binary experiences stable thermal-timescale Roche lobe overflow after the end of

the main sequence of the donor (i.e., case B type mass transfer).

The accretor compares well with observations of  $\zeta$  Oph about 1.5 – 2 Myrs after the end of mass transfer, corresponding to the remaining donor’s lifetime at the end of our simulations plus the kinematic age of  $\zeta$  Oph. Specifically, the position on the HR diagram (cf. Fig. 1), the runaway space velocity (estimated based on the accretor’s orbital velocity), the surface composition and rotational velocity (cf. Tab. 1) are in the right ballpark.

Our model of  $\zeta$  Oph differs significantly from previous studies: in contrast with the accretor models of van Rensbergen et al. (1996), in our model the  $^{14}\text{N}$ - and  $^4\text{He}$ -rich surface composition is not the result of pure outward rotational mixing. In addition, this material is transferred from the layers above the core of the donor star and mixed from the surface inwards into the accretor by meridional circulations and, more importantly, thermohaline mixing. Thus, the present day surface mass fractions of  $\zeta$  Oph constrain the mass transfer efficiency and mixing in the accretor. Our results suggest  $\zeta$  Oph should not be used to calibrate models of rotational mixing in single star models.

We emphasize that the surface composition alone would not be a smoking-gun of a binary evolution history, especially given the large uncertainties in the treatment of rotation and mixing in stellar evolution models. In our models, the accretion of  $^{14}\text{N}$  from the donor star allows the accretor star to be simultaneously fast rotating and  $^{14}\text{N}$ -rich. Alternative scenarios where  $\zeta$  Oph evolved as a single, fast-rotating star require ad-hoc explanations for the runaway velocity, and have been shown by VH05 to struggle in reproducing surface mass fractions, apparent age, mass, and rotation rate simultaneously.

The surface rotation rate of the accretor post-mass-transfer is always higher than the rotation rate of single stars initialized with half-critical rotation, but might still be on the low side compared to  $\zeta$  Oph. However, the wind spin down might be overestimated in our models (weak wind problem, cf. Marcolino et al. 2009; Lucy 2012; Lagae et al. 2021).

We also tested the robustness of our fiducial model against variations in the initial parameters and algorithmic representation of physical phenomena, discussed in Sec. 7. Less massive accretors remain too cool throughout the evolution to be compatible with  $\zeta$  Oph, and initial mass ratios closer to unity lead to a more evolved accretor at the onset of mass transfer, again resulting in too cool temperatures. Increasing the donor’s initial mass might result in stripped stars unlikely to form a neutron star in their final SN explosion.

### 8.2. Accretors are not single rotating stars

Our models also highlight some general differences between accretors in massive binaries and stars evolving as single throughout their life. These might be important for several sub-fields of astrophysics, including asteroseismology, stellar populations, and time-domain and gravitational waves observations.

The first notable difference we find is the internal rotation profile. Single rotating stars are usually initialized as rigid rotators at birth, and throughout their evolution they spin down due to wind mass loss. Conversely, accretors are spun up later during their main sequence and from the surface inward. Moreover, for single stars, the maximum rotation rate, that is the one assumed at the beginning of the evolution, is poorly understood theoretically and observationally (e.g., Ramírez-Agudelo et al. 2013; Ramírez-Agudelo et al. 2015). Conversely, accretors in binaries reach critical rotation  $\omega/\omega_{\text{crit}} \simeq 1$  (e.g., Packet 1981). The later spin-up and higher achieved rotation rate allow the accretor star to remain a fast rotator until the end of its main sequence.

The angular momentum accreted at the surface of the accretor is transported into the core (by the Tayler-Spruit dynamo in our simulations). This results in a much faster rotating helium core at the end of the main sequence compared to single stars. Such a fast spinning helium core has potential implications for the final explosion and the resulting compact object born from the accretor star in an interacting binary system.

Finally, in our models, the accretion of mass leads to rejuvenation and also the formation of a off-center convective layer above the main-sequence core (cf. Fig. 5). The latter ultimately results in a sharper density drop at the core edge, and a flatter density profile close to the end of the main sequence (cf. Fig. 6). If physical, the presence of such a convective layer could in principle be probed using asteroseismology. Depending on how the accretor (and the binary) evolves in the future, this

difference could be crucial in determining the outcome of common envelope events between massive stars and compact objects.

Improving our understanding of the evolution of the initially less massive stars in massive binary systems is crucial for the upcoming large surveys, stellar kinematics, and for the understanding of the evolution of gravitational-wave progenitors in isolated binaries. Although presently single, the nearest O-type star to Earth,  $\zeta$  Oph, can be used as an anchor point for the modeling of accretors. Our models demonstrate that a broad agreement with observations can be achieved with standard stellar evolution assumptions. Future efforts should extend these models to a wider mass, period, mass ratio, and metallicity range to investigate the impact of binary evolution on the life, explosion, and afterlife of the secondary stars in massive binary systems.

*Software:* MESA (Paxton et al. 2011, 2013, 2015, 2018, 2019), mesaSDK (Townsend 2018), ipython/jupyter (Pérez & Granger 2007), matplotlib (Hunter 2007), mesaPlot (Farmer 2018), NumPy (van der Walt et al. 2011).

## ACKNOWLEDGMENTS

We are grateful to E. Zapartas, A. Jermyn, M. Cantiello, R. Neuhäuser, B. D. Metzger, S. Oey, and S. Justham for helpful discussions and feedback. We also thank P. Marchant for helpful guidance with the newe superadiabaticity reduction capabilities in MESA. Support for this work was provided by NASA through the NASA Hubble Fellowship Program grant #HST-HF2-51457.001-A awarded by the Space Telescope Science Institute, which is operated by the Association of Universities for Research in Astronomy, Inc., for NASA, under contract NAS5-26555.

## APPENDIX

### A. MESA SETUP

We use MESA version 15140 to compute our models. The MESA equation of state (EOS) is a blend of the OPAL Rogers & Nayfonov (2002), SCVH Saumon et al. (1995), PTEH Pols et al. (1995), HELM Timmes & Swesty (2000), and PC Potekhin & Chabrier (2010) EOSes.

OPAL (Iglesias & Rogers 1993, 1996) provides the main radiative opacities, with low-temperature data from Ferguson et al. (2005) and the high-temperature

from Buchler & Yueh (1976). Electron conduction opacities are from Cassisi et al. (2007).

Nuclear reaction rates are a combination of rates from NACRE (Angulo et al. 1999), JINA REACLIB (Cyburt et al. 2010), plus additional tabulated weak reaction rates Fuller et al. (1985); Oda et al. (1994); Langanke & Martínez-Pinedo (2000). Screening is included via the prescription of Chugunov et al. (2007). Thermal neutrino loss rates are from Itoh et al. (1996). We use a 22-isotope nuclear network (`approx_21_plus_cr56`).

The inlists, processing scripts, and model output are available at <https://doi.org/10.5281/zenodo.4701565>.

## B. RESOLUTION TESTS

We extensively checked the numerical convergence of our stellar evolution calculations with increasing number of mesh points. Fig. 8 shows that all the main features described here do not vary when increasing the spatial resolution by increasing the number of mesh points (i.e., decreasing `mesh_delta_coeff`). The right panel shows the number of mesh points for the accretor (top) and donor (bottom) as a function of the model number (akin to an arbitrary time coordinate). About  $\sim 7000$  MESA timesteps are used to compute the binary evolution. The higher resolution run has  $\sim 20\%$  more mesh points. The left panel shows the evolution on the HR diagram until the detachment of the binary for the two accretor models (pink/red) and the two donor models (blue/cyan).

Similarly, we tested the numerical convergence with decreasing timestep size. This can be done decreasing the parameter `mesh_time_coeff`. However, we were unable to successfully compute models at higher temporal resolution. Partial results show a good agreement with our fiducial model until MESA becomes unable to find a satisfying numerical solution to the stellar structure equations (typically during RLOF). Lower temporal resolution models showed a similar qualitative agreement but increased noisiness during the late RLOF phase. For

our fiducial model the adaptive timestep size never exceeds  $10^{3.8}$  years with typical pre-RLOF timesteps of the order of  $10^{3.2}$  years and sub-decade (occasionally sub-year) during RLOF. The main factor limiting the timestep sizes is the change of surface angular momentum in both stars during the mass transfer.

## C. INTERNAL COMPOSITION PROFILE EVOLUTION AND MIXING

Fig. 9 compares the internal evolution of the composition profile of single rotating stars with our accretor model. We show mass fractions of  $^4\text{He}$ ,  $^{12}\text{C}$ , and  $^{16}\text{O}$  to complement the mass fraction of  $^{14}\text{N}$  shown in Fig. 7, and reproduced also in **third row** of Fig. 9. **The black error bars in the leftmost panel correspond to the abundances reported by VH05 assuming a surface hydrogen mass fraction  $X_{\text{surf}} = 0.67801$  (cf. Tab. 1).**

**Fig. 10 shows the composition profile of  $^1\text{H}$ ,  $^4\text{He}$ ,  $^{12}\text{C}$ ,  $^{14}\text{N}$ , and  $^{16}\text{O}$  for our fiducial accretor model shortly after ZAMS. The associated animation shows this evolves in time, as the core burning proceeds, mass is accreted during RLOF and mixed inwards.**

**Fig. 11 shows the diffusion coefficients for various mixing processes (cf. Fig. 5) at ZAMS. The associated animation shows the evolution of these mixing coefficients throughout our simulation until TAMS.**

## REFERENCES

- Almeida, L. A., Sana, H., Taylor, W., et al. 2017, A&A, 598, A84, doi: [10.1051/0004-6361/201629844](https://doi.org/10.1051/0004-6361/201629844)
- Angulo, C., Arnould, M., Rayet, M., et al. 1999, Nuclear Physics A, 656, 3, doi: [10.1016/S0375-9474\(99\)00030-5](https://doi.org/10.1016/S0375-9474(99)00030-5)
- Arnett, W. D. 1969, Ap&SS, 5, 180, doi: [10.1007/BF00650291](https://doi.org/10.1007/BF00650291)
- Asplund, M., Grevesse, N., Sauval, A. J., & Scott, P. 2009, ARA&A, 47, 481, doi: [10.1146/annurev.astro.46.060407.145222](https://doi.org/10.1146/annurev.astro.46.060407.145222)
- Belczynski, K., Holz, D. E., Bulik, T., & O'Shaughnessy, R. 2016, Nature, 534, 512, doi: [10.1038/nature18322](https://doi.org/10.1038/nature18322)
- Björklund, R., Sundqvist, J. O., Puls, J., & Najarro, F. 2021, A&A, 648, A36, doi: [10.1051/0004-6361/202038384](https://doi.org/10.1051/0004-6361/202038384)
- Blaauw, A. 1952, BAN, 11, 414
- . 1961, BAN, 15, 265
- Blaauw, A. 1993, in Astronomical Society of the Pacific Conference Series, Vol. 35, Massive Stars: Their Lives in the Interstellar Medium, ed. J. P. Cassinelli & E. B. Churchwell, 207
- Blagorodnova, N., Klencki, J., Pejcha, O., et al. 2021, arXiv e-prints, arXiv:2102.05662. <https://arxiv.org/abs/2102.05662>
- Bodensteiner, J., Baade, D., Greiner, J., & Langer, N. 2018, A&A, 618, A110, doi: [10.1051/0004-6361/201832722](https://doi.org/10.1051/0004-6361/201832722)
- Bodensteiner, J., Shenar, T., & Sana, H. 2020, A&A, 641, A42, doi: [10.1051/0004-6361/202037640](https://doi.org/10.1051/0004-6361/202037640)
- Boubert, D., & Evans, N. W. 2018. <https://arxiv.org/abs/1804.05849>
- Braun, H., & Langer, N. 1995, A&A, 297, 483
- Broekgaarden, F. S., Berger, E., Neijssel, C. J., et al. 2021, arXiv e-prints, arXiv:2103.02608. <https://arxiv.org/abs/2103.02608>
- Brott, I., de Mink, S. E., Cantiello, M., et al. 2011, A&A, 530, A115, doi: [10.1051/0004-6361/201016113](https://doi.org/10.1051/0004-6361/201016113)
- Buchler, J. R., & Yueh, W. R. 1976, ApJ, 210, 440, doi: [10.1086/154847](https://doi.org/10.1086/154847)

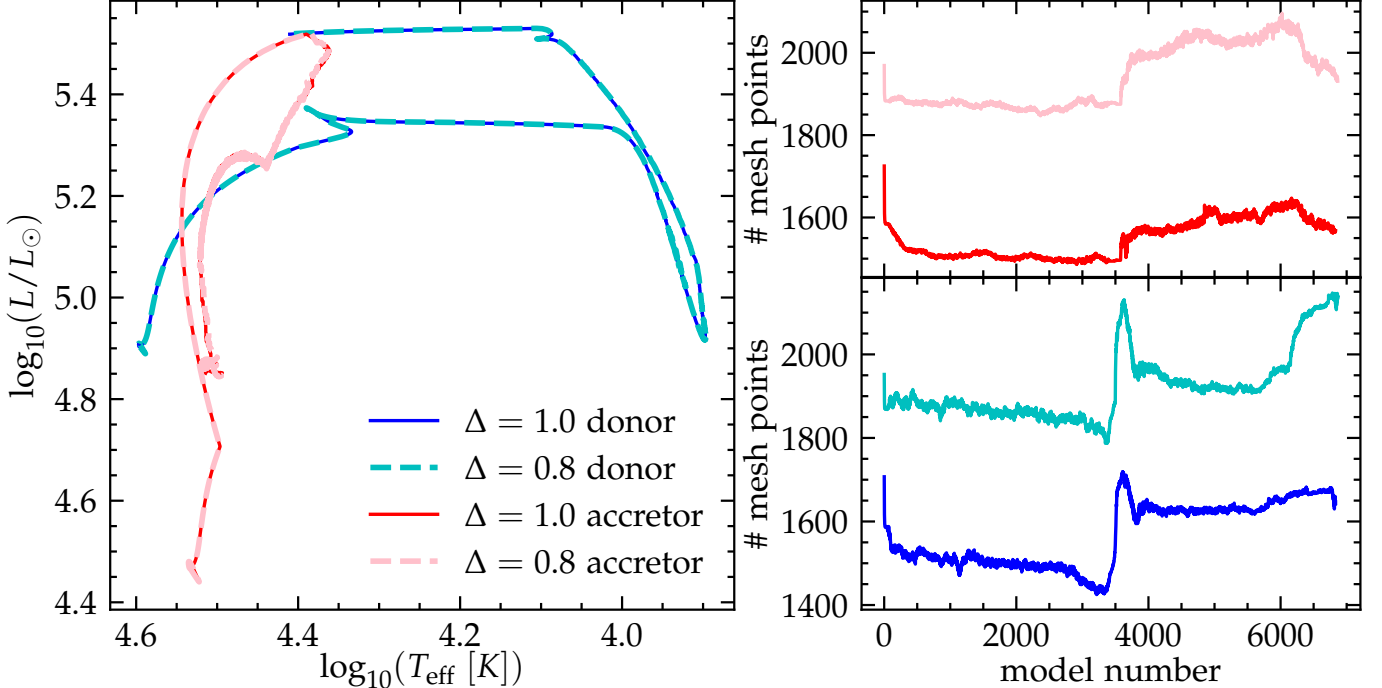


**Figure 8.** Left: HR diagram comparison for our fiducial binary model varying the number of mesh points. We only show the evolution until our definition of RLOF detachment. Right: number of mesh points as a function of timestep number. In both panels, the blue/cyan tracks show the donor stars, the red/pink tracks show the accretor. Thicker dashed lines correspond to the models at higher resolution (i.e., lower  $\Delta$  which indicates the value of `mesh_delta_coeff`).

- Callister, T. A., Farr, W. M., & Renzo, M. 2020, arXiv e-prints, arXiv:2011.09570.  
<https://arxiv.org/abs/2011.09570>
- Cantiello, M., Lecoanet, D., Jermyn, A. S., & Grassitelli, L. 2021, arXiv e-prints, arXiv:2102.05670.  
<https://arxiv.org/abs/2102.05670>
- Cantiello, M., Mankovich, C., Bildsten, L., Christensen-Dalsgaard, J., & Paxton, B. 2014, ApJ, 788, 93, doi: [10.1088/0004-637X/788/1/93](https://doi.org/10.1088/0004-637X/788/1/93)
- Cantiello, M., Yoon, S., Langer, N., & Livio, M. 2007, A&A, 465, L29
- Cassisi, S., Potekhin, A. Y., Pietrinferni, A., Catelan, M., & Salaris, M. 2007, ApJ, 661, 1094, doi: [10.1086/516819](https://doi.org/10.1086/516819)
- Chen, X., & Han, Z. 2009, MNRAS, 395, 1822, doi: [10.1111/j.1365-2966.2009.14669.x](https://doi.org/10.1111/j.1365-2966.2009.14669.x)
- . 2010, Ap&SS, 329, 277, doi: [10.1007/s10509-010-0368-0](https://doi.org/10.1007/s10509-010-0368-0)
- Chugunov, A. I., DeWitt, H. E., & Yakovlev, D. G. 2007, PhRvD, 76, 025028, doi: [10.1103/PhysRevD.76.025028](https://doi.org/10.1103/PhysRevD.76.025028)
- Claret, A., & Torres, G. 2017, ApJ, 849, 18, doi: [10.3847/1538-4357/aa8770](https://doi.org/10.3847/1538-4357/aa8770)
- Crowther, P. A. 2007, ARA&A, 45, 177, doi: [10.1146/annurev.astro.45.051806.110615](https://doi.org/10.1146/annurev.astro.45.051806.110615)
- Cyburt, R. H., Amthor, A. M., Ferguson, R., et al. 2010, ApJS, 189, 240, doi: [10.1088/0067-0049/189/1/240](https://doi.org/10.1088/0067-0049/189/1/240)

- De Donder, E., Vanbeveren, D., & van Bever, J. 1997, A&A, 318, 812
- de Jager, C., Nieuwenhuijzen, H., & van der Hucht, K. A. 1988, A&AS, 72, 259
- de Mink, S. E., Langer, N., & Izzard, R. G. 2011, Bulletin de la Societe Royale des Sciences de Liege, 80, 543.  
<https://arxiv.org/abs/1010.2200>
- de Mink, S. E., Langer, N., Izzard, R. G., Sana, H., & de Koter, A. 2013, ApJ, 764, 166, doi: [10.1088/0004-637X/764/2/166](https://doi.org/10.1088/0004-637X/764/2/166)
- Dorigo Jones, J., Oey, M. S., Paggeot, K., Castro, N., & Moe, M. 2020, ApJ, 903, 43, doi: [10.3847/1538-4357/abbc6b](https://doi.org/10.3847/1538-4357/abbc6b)
- Ekström, S., Georgy, C., Eggenberger, P., et al. 2012, A&A, 537, A146, doi: [10.1051/0004-6361/201117751](https://doi.org/10.1051/0004-6361/201117751)
- Eldridge, J. J., Langer, N., & Tout, C. A. 2011, MNRAS, 414, 3501, doi: [10.1111/j.1365-2966.2011.18650.x](https://doi.org/10.1111/j.1365-2966.2011.18650.x)
- Eldridge, J. J., & Stanway, E. R. 2012, MNRAS, 419, 479, doi: [10.1111/j.1365-2966.2011.19713.x](https://doi.org/10.1111/j.1365-2966.2011.19713.x)
- Evans, F. A., Renzo, M., & Rossi, E. M. 2020, arXiv e-prints, arXiv:2006.00849.  
<https://arxiv.org/abs/2006.00849>
- Farmer, R. 2018, rjfarmer/mesaplot, doi: [10.5281/zenodo.1441329](https://doi.org/10.5281/zenodo.1441329)

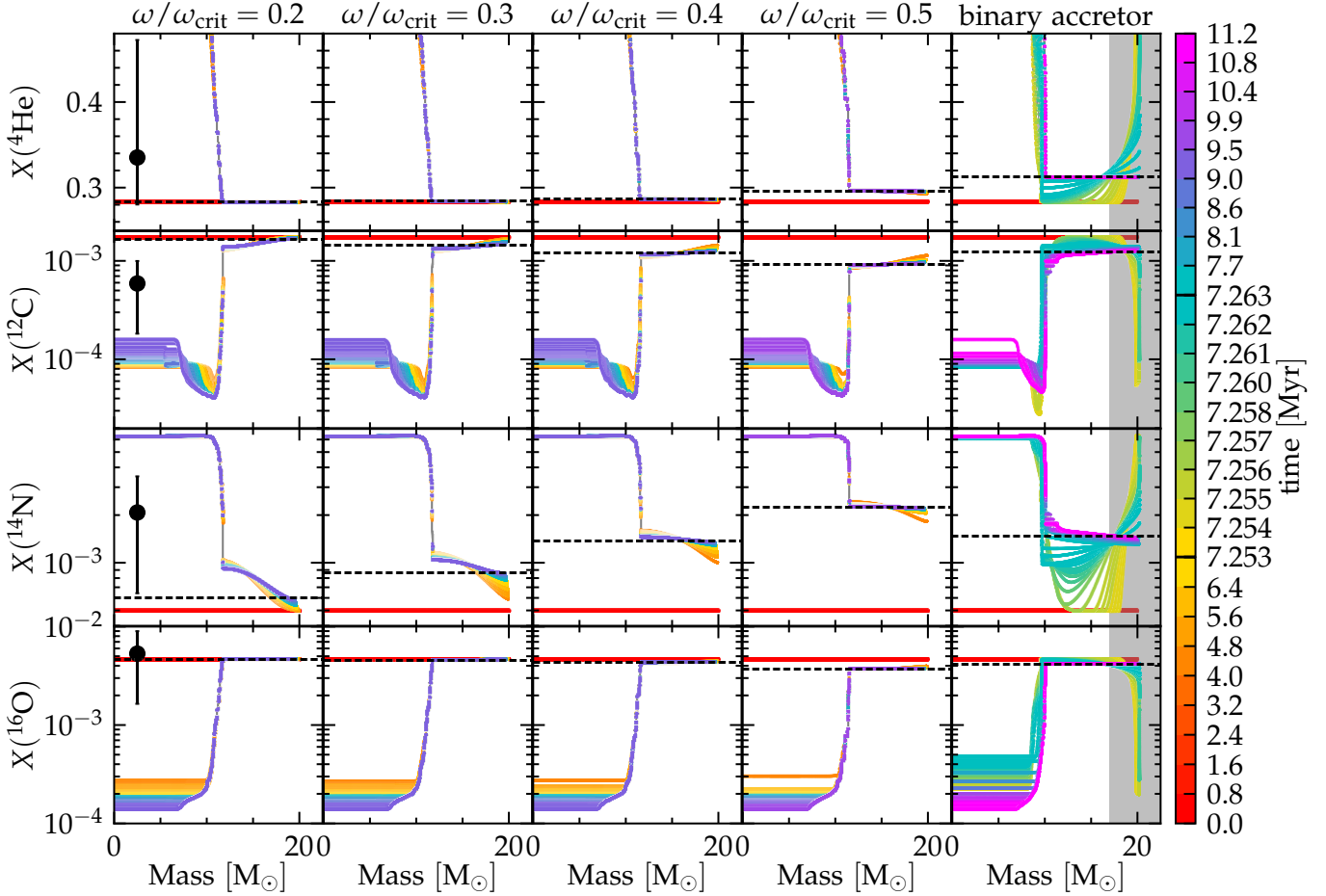


**Figure 9.** Same as Fig. 7, but for  ${}^4\text{He}$  (top row),  ${}^{12}\text{C}$  (second row),  ${}^{14}\text{N}$  (third row, identical to Fig. 7), and  ${}^{16}\text{O}$  (bottom row). We emphasize the linear scale on the vertical axis in the top row, while all others have a logarithmic scale. The first four panels show single rotating stars of initially  $20 M_{\odot}$ , the rightmost panels show the accretor in our fiducial binary. The red lines mark the initial mass fractions, black dashed lines indicate the TAMS surface mass fraction, and the black error bars in the first column indicate the surface composition of  $\zeta$  Oph inferred by VH05 using the surface H mass fraction from our model.

Ferguson, J. W., Alexander, D. R., Allard, F., et al. 2005, ApJ, 623, 585, doi: [10.1086/428642](https://doi.org/10.1086/428642)

Fuller, G. M., Fowler, W. A., & Newman, M. J. 1985, ApJ, 293, 1, doi: [10.1086/163208](https://doi.org/10.1086/163208)

Fuller, J., Piro, A. L., & Jermyn, A. S. 2019, MNRAS, 485, 3661, doi: [10.1093/mnras/stz514](https://doi.org/10.1093/mnras/stz514)

Gilkis, A., Vink, J. S., Eldridge, J. J., & Tout, C. A. 2019, MNRAS, 486, 4451, doi: [10.1093/mnras/stz1134](https://doi.org/10.1093/mnras/stz1134)

Gordon, K. D., Gies, D. R., Schaefer, G. H., et al. 2018, ApJ, 869, 37, doi: [10.3847/1538-4357/aaec04](https://doi.org/10.3847/1538-4357/aaec04)

Götberg, Y., de Mink, S. E., & Groh, J. H. 2017, <https://arxiv.org/abs/1701.07439>

Götberg, Y., de Mink, S. E., Groh, J. H., et al. 2018, A&A, 615, A78, doi: [10.1051/0004-6361/201732274](https://doi.org/10.1051/0004-6361/201732274)

Grasha, K., Roy, A., Sutherland, R. S., & Kewley, L. J. 2021, ApJ, 908, 241, doi: [10.3847/1538-4357/abd6bf](https://doi.org/10.3847/1538-4357/abd6bf)

Grevesse, N., & Sauval, A. J. 1998, SSRv, 85, 161, doi: [10.1023/A:1005161325181](https://doi.org/10.1023/A:1005161325181)

Hastings, B., Langer, N., Wang, C., Schootemeijer, A., & Milone, A. P. 2021, arXiv e-prints, arXiv:2106.12263, <https://arxiv.org/abs/2106.12263>

Heger, A., Langer, N., & Woosley, S. E. 2000, ApJ, 528, 368

Hellings, P. 1983, Ap&SS, 96, 37, doi: [10.1007/BF00661941](https://doi.org/10.1007/BF00661941)

—. 1984, Ap&SS, 104, 83, doi: [10.1007/BF00653994](https://doi.org/10.1007/BF00653994)

Herrero, A., Kudritzki, R. P., Vilchez, J. M., et al. 1992, A&A, 261, 209

Herwig, F. 2000, A&A, 360, 952

Hirai, R., Podsiadlowski, P., & Yamada, S. 2018, <https://arxiv.org/abs/1803.10808>

Hoogerwerf, R., de Bruijne, J. H. J., & de Zeeuw, P. T. 2000, ApJL, 544, L133, doi: [10.1086/317315](https://doi.org/10.1086/317315)

—. 2001, A&A, 365, 49, doi: [10.1051/0004-6361:20000014](https://doi.org/10.1051/0004-6361:20000014)

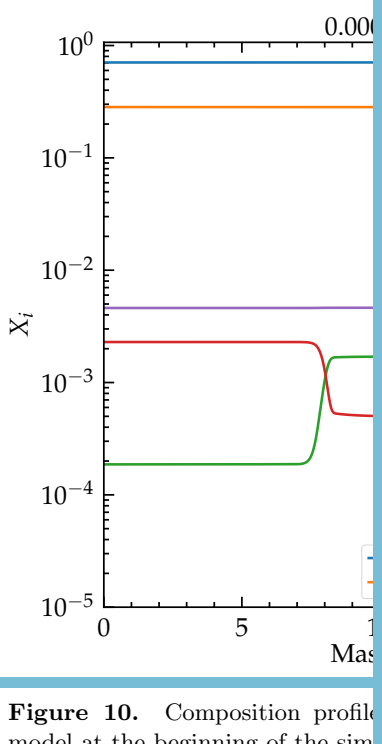


**Figure 10.** Composition profile model at the beginning of the sim

mation shows the entire main-sequence evolution (see physical time at the top). The number of frames per unit time is not constant, and greatly increases during the RLOF phase, when smaller timesteps are needed.

- Hunter, J. D. 2007, Computing In Science & Engineering, 9, 90
- Iglesias, C. A., & Rogers, F. J. 1993, ApJ, 412, 752, doi: [10.1086/172958](https://doi.org/10.1086/172958)
- . 1996, ApJ, 464, 943, doi: [10.1086/177381](https://doi.org/10.1086/177381)
- Itoh, N., Hayashi, H., Nishikawa, A., & Kohyama, Y. 1996, ApJS, 102, 411, doi: [10.1086/192264](https://doi.org/10.1086/192264)
- Kalogera, V. 1996, ApJ, 471, 352, doi: [10.1086/177974](https://doi.org/10.1086/177974)
- Kippenhahn, R., Ruschenplatt, G., & Thomas, H.-C. 1980, A&A, 91, 175
- Kippenhahn, R., & Weigert, A. 1967, ZA, 65, 251
- Klencki, J., Nelemans, G., Istrate, A. G., & Chruslinska, M. 2021, A&A, 645, A54, doi: [10.1051/0004-6361/202038707](https://doi.org/10.1051/0004-6361/202038707)
- Klencki, J., Nelemans, G., Istrate, A. G., & Pols, O. 2020, A&A, 638, A55, doi: [10.1051/0004-6361/202037694](https://doi.org/10.1051/0004-6361/202037694)
- Kolb, U., & Ritter, H. 1990, A&A, 236, 385
- Lagae, C., Driessen, F. A., Hennicker, L., Kee, N. D., & Sundqvist, J. O. 2021, arXiv e-prints, arXiv:2103.15904. <https://arxiv.org/abs/2103.15904>
- Langanke, K., & Martínez-Pinedo, G. 2000, Nuclear Physics A, 673, 481, doi: [10.1016/S0375-9474\(00\)00131-7](https://doi.org/10.1016/S0375-9474(00)00131-7)
- Langer, N. 1998, A&A, 329, 551

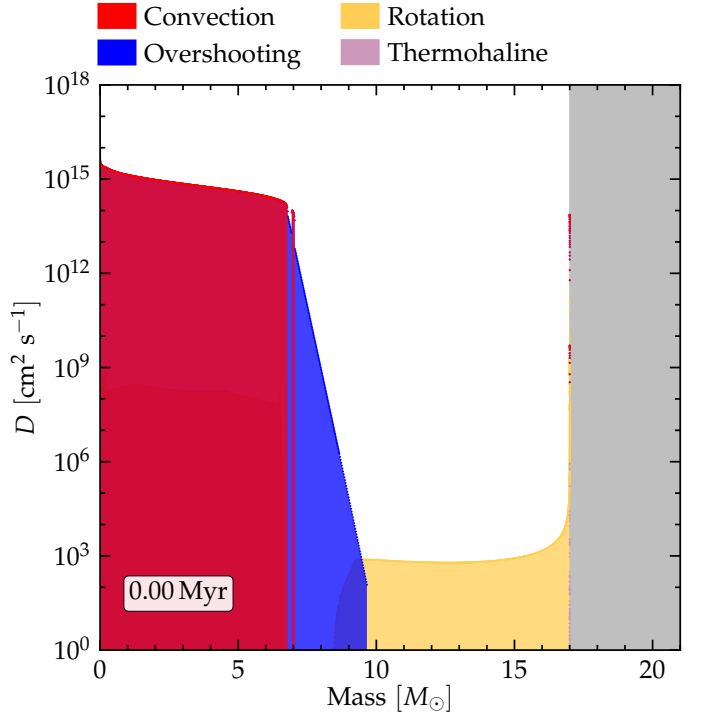


**Figure 11.** Diffusion coefficients for convection (red), overshooting (blue), thermohaline (pink), and rotational mixing (yellow). The latter includes meridional circulations, secular and dynamical shear, and GSF. Semiconvection is not shown for clarity. The associated animation shows how these evolve with time until TAMS. The number of frames per unit time is not constant, and greatly increases during the RLOF phase, when smaller timesteps are needed.

- Langer, N., Fricke, K. J., & Sugimoto, D. 1983, A&A, 126, 207
- Laplace, E., Götberg, Y., de Mink, S. E., Justham, S., & Farmer, R. 2020, A&A, 637, A6, doi: [10.1051/0004-6361/201937300](https://doi.org/10.1051/0004-6361/201937300)
- Laplace, E., Justham, S., Renzo, M., et al. 2021, arXiv e-prints, arXiv:2102.05036. <https://arxiv.org/abs/2102.05036>
- Law-Smith, J. A. P., Everson, R. W., Ramirez-Ruiz, E., et al. 2020, arXiv e-prints, arXiv:2011.06630. <https://arxiv.org/abs/2011.06630>
- Ledoux, P. 1947, ApJ, 105, 305, doi: [10.1086/144905](https://doi.org/10.1086/144905)
- Lodders, K. 2019, arXiv e-prints, arXiv:1912.00844. <https://arxiv.org/abs/1912.00844>
- Lubow, S. H., & Shu, F. H. 1975, ApJ, 198, 383, doi: [10.1086/153614](https://doi.org/10.1086/153614)
- Lucy, L. B. 2012, A&A, 544, A120, doi: [10.1051/0004-6361/201118753](https://doi.org/10.1051/0004-6361/201118753)
- MacFadyen, A. I., & Woosley, S. E. 1999, ApJ, 524, 262

- Maeder, A., & Meynet, G. 2000, *ARA&A*, 38, 143, doi: [10.1146/annurev.astro.38.1.143](https://doi.org/10.1146/annurev.astro.38.1.143)
- Marcolino, W. L. F., Bouret, J. C., Martins, F., et al. 2009, *A&A*, 498, 837, doi: [10.1051/0004-6361/200811289](https://doi.org/10.1051/0004-6361/200811289)
- Mason, B. D., Hartkopf, W. I., Gies, D. R., Henry, T. J., & Helsel, J. W. 2009, *AJ*, 137, 3358, doi: [10.1088/0004-6256/137/2/3358](https://doi.org/10.1088/0004-6256/137/2/3358)
- Massey, P., Neugent, K. F., Morrell, N., & Hillier, D. J. 2014, *ApJ*, 788, 83, doi: [10.1088/0004-637X/788/1/83](https://doi.org/10.1088/0004-637X/788/1/83)
- Meynet, G., & Maeder, A. 2000, *A&A*, 361, 101 —. 2003, *A&A*, 404, 975, doi: [10.1051/0004-6361:20030512](https://doi.org/10.1051/0004-6361:20030512)
- Moe, M., & Di Stefano, R. 2017, *ApJS*, 230, 15, doi: [10.3847/1538-4365/aa6fb6](https://doi.org/10.3847/1538-4365/aa6fb6)
- Moravveji, E., Townsend, R. H. D., Aerts, C., & Mathis, S. 2016, *ApJ*, 823, 130, doi: [10.3847/0004-637X/823/2/130](https://doi.org/10.3847/0004-637X/823/2/130)
- Morton, D. C. 1960, *ApJ*, 132, 146, doi: [10.1086/146908](https://doi.org/10.1086/146908)
- Murphy, S. J., Joyce, M., Bedding, T. R., White, T. R., & Kama, M. 2021, *MNRAS*, 502, 1633, doi: [10.1093/mnras/stab144](https://doi.org/10.1093/mnras/stab144)
- Neo, S., Miyaji, S., Nomoto, K., & Sugimoto, D. 1977, *PASJ*, 29, 249
- Neugent, K. F., Massey, P., Hillier, D. J., & Morrell, N. 2017, *ApJ*, 841, 20, doi: [10.3847/1538-4357/aa6e51](https://doi.org/10.3847/1538-4357/aa6e51)
- Neuhäuser, R., Gießler, F., & Hambaryan, V. V. 2020, *MNRAS*, 498, 899, doi: [10.1093/mnras/stz2629](https://doi.org/10.1093/mnras/stz2629)
- Nugis, T., & Lamers, H. J. G. L. M. 2000, *A&A*, 360, 227
- Oda, T., Hino, M., Muto, K., Takahara, M., & Sato, K. 1994, *Atomic Data and Nuclear Data Tables*, 56, 231, doi: [10.1006/adnd.1994.1007](https://doi.org/10.1006/adnd.1994.1007)
- Ogata, M., Hirai, R., & Hijikawa, K. 2021, *MNRAS*, 505, 2485, doi: [10.1093/mnras/stab1439](https://doi.org/10.1093/mnras/stab1439)
- Packet, W. 1981, *A&A*, 102, 17
- Paczynski, B. 1976, in *IAU Symposium*, Vol. 73, Structure and Evolution of Close Binary Systems, ed. P. Eggleton, S. Mitton, & J. Whelan, 75
- Paczynski, B. 1991, *ApJ*, 370, 597, doi: [10.1086/169846](https://doi.org/10.1086/169846)
- Paxton, B., Bildsten, L., Dotter, A., et al. 2011, *ApJS*, 192, 3, doi: [10.1088/0067-0049/192/1/3](https://doi.org/10.1088/0067-0049/192/1/3)
- Paxton, B., Cantiello, M., Arras, P., et al. 2013, *ApJS*, 208, 4, doi: [10.1088/0067-0049/208/1/4](https://doi.org/10.1088/0067-0049/208/1/4)
- Paxton, B., Marchant, P., Schwab, J., et al. 2015, *ApJS*, 220, 15, doi: [10.1088/0067-0049/220/1/15](https://doi.org/10.1088/0067-0049/220/1/15)
- Paxton, B., Schwab, J., Bauer, E. B., et al. 2018, *ApJS*, 234, 34, doi: [10.3847/1538-4365/aaa5a8](https://doi.org/10.3847/1538-4365/aaa5a8)
- Paxton, B., Smolec, R., Gautschy, A., et al. 2019. <https://arxiv.org/abs/1903.01426>
- Pecaut, M. J., & Mamajek, E. E. 2016, *MNRAS*, 461, 794, doi: [10.1093/mnras/stw1300](https://doi.org/10.1093/mnras/stw1300)
- Pérez, F., & Granger, B. E. 2007, Computing in Science & Engineering, 9, 21
- Perna, R., Duffell, P., Cantiello, M., & MacFadyen, A. I. 2014, *ApJ*, 781, 119, doi: [10.1088/0004-637X/781/2/119](https://doi.org/10.1088/0004-637X/781/2/119)
- Petrovic, J., Langer, N., & van der Hucht, K. A. 2005, *A&A*, 435, 1013, doi: [10.1051/0004-6361:20042368](https://doi.org/10.1051/0004-6361:20042368)
- Podsiadlowski, P. 2003, arXiv e-prints, astro. <https://arxiv.org/abs/astro-ph/0303660>
- Pols, O. R., Cote, J., Waters, L. B. F. M., & Heise, J. 1991, *A&A*, 241, 419
- Pols, O. R., & Marinus, M. 1994, *A&A*, 288, 475
- Pols, O. R., Tout, C. A., Eggleton, P. P., & Han, Z. 1995, *MNRAS*, 274, 964, doi: [10.1093/mnras/274.3.964](https://doi.org/10.1093/mnras/274.3.964)
- Popham, R., & Narayan, R. 1991, *ApJ*, 370, 604, doi: [10.1086/169847](https://doi.org/10.1086/169847)
- Potekhin, A. Y., & Chabrier, G. 2010, Contributions to Plasma Physics, 50, 82, doi: [10.1002/ctpp.201010017](https://doi.org/10.1002/ctpp.201010017)
- Przybilla, N., Nieva, M. F., Heber, U., & Butler, K. 2008, *The Astrophysical Journal*, 684, L103, doi: [10.1086/592245](https://doi.org/10.1086/592245)
- Qin, Y., Fragos, T., Meynet, G., et al. 2018, *A&A*, 616, A28, doi: [10.1051/0004-6361/201832839](https://doi.org/10.1051/0004-6361/201832839)
- Rain, M. J., Ahumada, J., & Carraro, G. 2021, arXiv e-prints, arXiv:2103.06004. <https://arxiv.org/abs/2103.06004>
- Ramírez-Agudelo, O. H., Simón-Díaz, S., Sana, H., et al. 2013, *A&A*, 560, A29, doi: [10.1051/0004-6361/201321986](https://doi.org/10.1051/0004-6361/201321986)
- Ramírez-Agudelo, O. H., Sana, H., de Mink, S. E., et al. 2015, *A&A*, 580, A92, doi: [10.1051/0004-6361/201425424](https://doi.org/10.1051/0004-6361/201425424)
- Renzo, M., Farmer, R. J., Justham, S., et al. 2020, arXiv e-prints, arXiv:2002.08200. <https://arxiv.org/abs/2002.08200>
- Renzo, M., Ott, C. D., Shore, S. N., & de Mink, S. E. 2017, *A&A*, 603, A118, doi: [10.1051/0004-6361/201730698](https://doi.org/10.1051/0004-6361/201730698)
- Renzo, M., Zapartas, E., de Mink, S. E., et al. 2019, *A&A*, 624, A66, doi: [10.1051/0004-6361/201833297](https://doi.org/10.1051/0004-6361/201833297)
- Rivinius, T., Carciofi, A. C., & Martayan, C. 2013, *A&A Rv*, 21, 69, doi: [10.1007/s00159-013-0069-0](https://doi.org/10.1007/s00159-013-0069-0)
- Rogers, F. J., & Nayfonov, A. 2002, *ApJ*, 576, 1064, doi: [10.1086/341894](https://doi.org/10.1086/341894)
- Sana, H., de Mink, S. E., de Koter, A., et al. 2012, *Science*, 337, 444, doi: [10.1126/science.1223344](https://doi.org/10.1126/science.1223344)
- Sander, A. A. C., & Vink, J. S. 2020, *MNRAS*, 499, 873, doi: [10.1093/mnras/staa2712](https://doi.org/10.1093/mnras/staa2712)
- Saumon, D., Chabrier, G., & van Horn, H. M. 1995, *ApJS*, 99, 713, doi: [10.1086/192204](https://doi.org/10.1086/192204)
- Schneider, F. R. N., Izzard, R. G., Langer, N., & de Mink, S. E. 2015, *ApJ*, 805, 20, doi: [10.1088/0004-637X/805/1/20](https://doi.org/10.1088/0004-637X/805/1/20)
- Schneider, F. R. N., Podsiadlowski, P., Langer, N., Castro, N., & Fossati, L. 2016, *MNRAS*, 457, 2355, doi: [10.1093/mnras/stw148](https://doi.org/10.1093/mnras/stw148)

- Schneider, F. R. N., Podsiadlowski, P., & Müller, B. 2021, A&A, 645, A5, doi: [10.1051/0004-6361/202039219](https://doi.org/10.1051/0004-6361/202039219)
- Schootemeijer, A., Langer, N., Grin, N. J., & Wang, C. 2019, A&A, 625, A132, doi: [10.1051/0004-6361/201935046](https://doi.org/10.1051/0004-6361/201935046)
- Shenar, T., Gilkis, A., Vink, J. S., Sana, H., & Sander, A. A. C. 2020, A&A, 634, A79, doi: [10.1051/0004-6361/201936948](https://doi.org/10.1051/0004-6361/201936948)
- Smith, N. 2014, ARA&A, 52, 487, doi: [10.1146/annurev-astro-081913-040025](https://doi.org/10.1146/annurev-astro-081913-040025)
- Soberman, G. E., Phinney, E. S., & van den Heuvel, E. P. J. 1997, A&A, 327, 620
- Sota, A., Maíz Apellániz, J., Morrell, N. I., et al. 2014, ApJS, 211, 10, doi: [10.1088/0067-0049/211/1/10](https://doi.org/10.1088/0067-0049/211/1/10)
- Spruit, H. C. 2002, A&A, 381, 923, doi: [10.1051/0004-6361:20011465](https://doi.org/10.1051/0004-6361:20011465)
- Sravan, N., Marchant, P., & Kalogera, V. 2019, ApJ, 885, 130, doi: [10.3847/1538-4357/ab4ad7](https://doi.org/10.3847/1538-4357/ab4ad7)
- Stanway, E. R., Eldridge, J. J., & Becker, G. D. 2016, MNRAS, 456, 485, doi: [10.1093/mnras/stv2661](https://doi.org/10.1093/mnras/stv2661)
- Suda, T., Saitoh, T. R., Moritani, Y., Matsuno, T., & Shigeyama, T. 2021, arXiv e-prints, arXiv:2103.13627. <https://arxiv.org/abs/2103.13627>
- Sweet, P. A. 1950, MNRAS, 110, 548, doi: [10.1093/mnras/110.6.548](https://doi.org/10.1093/mnras/110.6.548)
- Tauris, T. M. 2015, MNRAS, 448, L6, doi: [10.1093/mnrasl/slu189](https://doi.org/10.1093/mnrasl/slu189)
- Tauris, T. M., & Takens, R. J. 1998, A&A, 330, 1047
- Tauris, T. M., Kramer, M., Freire, P. C. C., et al. 2017, ApJ, 846, 170, doi: [10.3847/1538-4357/aa7e89](https://doi.org/10.3847/1538-4357/aa7e89)
- Tetzlaff, N., Neuhauser, R., Hohle, M. M., & Maciejewski, G. 2010, MNRAS, 402, 2369, doi: [10.1111/j.1365-2966.2009.16093.x](https://doi.org/10.1111/j.1365-2966.2009.16093.x)
- Timmes, F. X., & Swesty, F. D. 2000, ApJS, 126, 501, doi: [10.1086/313304](https://doi.org/10.1086/313304)
- Townsend, R. 2018, MESA SDK for Linux: 20180822, doi: [10.5281/zenodo.2603170](https://doi.org/10.5281/zenodo.2603170)
- Ulrich, R. K., & Burger, H. L. 1976, ApJ, 206, 509, doi: [10.1086/154406](https://doi.org/10.1086/154406)
- van den Heuvel, E. P. J., Portegies Zwart, S. F., & de Mink, S. E. 2017, MNRAS, 471, 4256, doi: [10.1093/mnras/stx1430](https://doi.org/10.1093/mnras/stx1430)
- van der Walt, S., Colbert, S. C., & Varoquaux, G. 2011, Computing in Science Engineering, 13, 22, doi: [10.1109/MCSE.2011.37](https://doi.org/10.1109/MCSE.2011.37)
- van Rensbergen, W., de Greve, J. P., Mennekens, N., Jansen, K., & de Loore, C. 2011, A&A, 528, A16, doi: [10.1051/0004-6361/201015596](https://doi.org/10.1051/0004-6361/201015596)
- van Rensbergen, W., De Loore, C., & Jansen, K. 2006, A&A, 446, 1071, doi: [10.1051/0004-6361:20053543](https://doi.org/10.1051/0004-6361:20053543)
- van Rensbergen, W., Vanbeveren, D., & De Loore, C. 1996, A&A, 305, 825
- Vartanyan, D., Laplace, E., Renzo, M., et al. 2021, arXiv e-prints, arXiv:2104.03317. <https://arxiv.org/abs/2104.03317>
- Villamariz, M. R., & Herrero, A. 2005, A&A, 442, 263, doi: [10.1051/0004-6361:20052848](https://doi.org/10.1051/0004-6361:20052848)
- Vinciguerra, S., Neijssel, C. J., Vigna-Gómez, A., et al. 2020, MNRAS, 498, 4705, doi: [10.1093/mnras/staa2177](https://doi.org/10.1093/mnras/staa2177)
- Vink, J. S. 2017, A&A, 607, L8, doi: [10.1051/0004-6361/201731902](https://doi.org/10.1051/0004-6361/201731902)
- Vink, J. S., Davies, B., Harries, T. J., Oudmaijer, R. D., & Walborn, N. R. 2009, A&A, 505, 743, doi: [10.1051/0004-6361/200912610](https://doi.org/10.1051/0004-6361/200912610)
- Vink, J. S., de Koter, A., & Lamers, H. J. G. L. M. 2000, A&A, 362, 295
- . 2001, A&A, 369, 574, doi: [10.1051/0004-6361:20010127](https://doi.org/10.1051/0004-6361:20010127)
- Walker, G. A. H., Yang, S., & Fahlman, G. G. 1979, ApJ, 233, 199, doi: [10.1086/157381](https://doi.org/10.1086/157381)
- Walker, G. A. H., Kuschnig, R., Matthews, J. M., et al. 2005, ApJL, 623, L145, doi: [10.1086/430254](https://doi.org/10.1086/430254)
- Wang, C., Langer, N., Schootemeijer, A., et al. 2020, ApJL, 888, L12, doi: [10.3847/2041-8213/ab6171](https://doi.org/10.3847/2041-8213/ab6171)
- Wang, L., Gies, D. R., Peters, G. J., et al. 2021, arXiv e-prints, arXiv:2103.13642. <https://arxiv.org/abs/2103.13642>
- Wei, D., Wang, B., Chen, H., et al. 2021, arXiv e-prints, arXiv:2105.00291. <https://arxiv.org/abs/2105.00291>
- Wheeler, J. C., Lecar, M., & McKee, C. F. 1975, ApJ, 200, 145, doi: [10.1086/153771](https://doi.org/10.1086/153771)
- Yoon, S.-C., Dessart, L., & Clocchiatti, A. 2017, ApJ, 840, 10, doi: [10.3847/1538-4357/aa6afe](https://doi.org/10.3847/1538-4357/aa6afe)
- Yoon, S.-C., Langer, N., & Norman, C. 2006, A&A, 460, 199, doi: [10.1051/0004-6361:20065912](https://doi.org/10.1051/0004-6361:20065912)
- Zahn, J. P. 1992, A&A, 265, 115
- Zaldarriaga, M., Kushnir, D., & Kollmeier, J. A. 2018, MNRAS, 473, 4174, doi: [10.1093/mnras/stx2577](https://doi.org/10.1093/mnras/stx2577)
- Zapartas, E., de Mink, S. E., Justham, S., et al. 2021, A&A, 645, A6, doi: [10.1051/0004-6361/202037744](https://doi.org/10.1051/0004-6361/202037744)
- . 2019. <https://arxiv.org/abs/1907.06687>
- Zehe, T., Mugrauer, M., Neuhauser, R., et al. 2018, Astronomische Nachrichten, 339, 46, doi: [10.1002/asna.201713383](https://doi.org/10.1002/asna.201713383)
- Zhao, X., & Fuller, J. 2020, MNRAS, 495, 249, doi: [10.1093/mnras/staa1097](https://doi.org/10.1093/mnras/staa1097)